

AD_____

AWARD NUMBER: W81XWH-06-1-0732

TITLE: Temporal Subtraction of Digital Breast Tomosynthesis Images for Improved Mass Detection

PRINCIPAL INVESTIGATOR: Christina M. Li
James T. Dobbins, III, Ph.D.

CONTRACTING ORGANIZATION: Duke University
Durham, NC 27708

REPORT DATE: November 2009

TYPE OF REPORT: Annual Summary

PREPARED FOR: U.S. Army Medical Research and Materiel Command
Fort Detrick, Maryland 21702-5012

DISTRIBUTION STATEMENT: Approved for Public Release;
Distribution Unlimited

The views, opinions and/or findings contained in this report are those of the author(s) and should not be construed as an official Department of the Army position, policy or decision unless so designated by other documentation.

REPORT DOCUMENTATION PAGE				Form Approved OMB No. 0704-0188	
Public reporting burden for this collection of information is estimated to average 1 hour per response, including the time for reviewing instructions, searching existing data sources, gathering and maintaining the data needed, and completing and reviewing this collection of information. Send comments regarding this burden estimate or any other aspect of this collection of information, including suggestions for reducing this burden to Department of Defense, Washington Headquarters Services, Directorate for Information Operations and Reports (0704-0188), 1215 Jefferson Davis Highway, Suite 1204, Arlington, VA 22202-4302. Respondents should be aware that notwithstanding any other provision of law, no person shall be subject to any penalty for failing to comply with a collection of information if it does not display a currently valid OMB control number. PLEASE DO NOT RETURN YOUR FORM TO THE ABOVE ADDRESS.					
1. REPORT DATE 1 November 2009		2. REPORT TYPE Annual Summary		3. DATES COVERED 15 Sep 2006 – 14 Oct 2009	
4. TITLE AND SUBTITLE Temporal Subtraction of Digital Breast Tomosynthesis Images for Improved Mass Detection				5a. CONTRACT NUMBER	
				5b. GRANT NUMBER W81XWH-06-1-0732	
				5c. PROGRAM ELEMENT NUMBER	
6. AUTHOR(S) Christina M. Li; James T. Dobbins, III, Ph.D. E-Mail: christina.li@duke.edu				5d. PROJECT NUMBER	
				5e. TASK NUMBER	
				5f. WORK UNIT NUMBER	
7. PERFORMING ORGANIZATION NAME(S) AND ADDRESS(ES) Duke University Durham, NC 2 7708				8. PERFORMING ORGANIZATION REPORT NUMBER	
9. SPONSORING / MONITORING AGENCY NAME(S) AND ADDRESS(ES) U.S. Army Medical Research and Materiel Command Fort Detrick, Maryland 21702-5012				10. SPONSOR/MONITOR'S ACRONYM(S)	
				11. SPONSOR/MONITOR'S REPORT NUMBER(S)	
12. DISTRIBUTION / AVAILABILITY STATEMENT Approved for Public Release; Distribution Unlimited					
13. SUPPLEMENTARY NOTES					
14. ABSTRACT The original goal of this project was to combine two methods developed to increase the sensitivity of breast cancer imaging - digital breast tomosynthesis (DBT) and temporal subtraction. The combined technique would allow for easier and earlier detection of breast cancer than with either technique alone. Although the original scope of the project outlined using computer simulations and physical phantoms to evaluate the feasibility of the method, an IRB approved initial investigation was performed using temporally acquired DBT images of human subjects. The results showed that structural discrepancies, due to differences in positioning and compression between temporally spaced acquisitions, caused slight anatomical variations between reconstructed slices that significantly reduced registration accuracy and subtraction. Although, the feasibility of combining the two methods using simulation and physical phantoms may have shown to be promising, the initial results using actual human subject data did not indicate a significant improvement in breast cancer detection. These results prompted the change in scope of the project to focus on developing a realistic computerized breast phantom (RCBP) to be used for breast imaging research. The RCBP can be used for simulations that study imaging system design, acquisition protocols, reconstruction algorithms, and image processing techniques. The phantom developed in this project will provide a vital tool to investigate current and emerging breast imaging methods and techniques with the ability to simulate realistic, predictive patient imaging data.					
15. SUBJECT TERMS Digital Breast Tomosynthesis, Temporal Subtraction, Breast Imaging, Computer Simulation, Phantoms					
16. SECURITY CLASSIFICATION OF:			17. LIMITATION OF ABSTRACT UU	18. NUMBER OF PAGES 32	19a. NAME OF RESPONSIBLE PERSON USAMRMC
a. REPORT U	b. ABSTRACT U	c. THIS PAGE U			19b. TELEPHONE NUMBER (include area code)

Contents

Introduction.....4

Body.....4

Key Research Accomplishments.....9

Reportable Outcomes.....9

Conclusions..... 10

References 10

Appendix..... 10

Introduction

The original goal of this project was to combine two methods developed to increase the sensitivity of breast cancer imaging - digital breast tomosynthesis (DBT) and temporal subtraction. The purpose of the project was to determine the feasibility of subtracting temporally spaced DBT images to highlight potentially significant changes in breast morphology between acquisitions. The combined technique would allow for easier and earlier detection of breast cancer than with either technique alone. Although the original scope of the project outlined using computer simulations and physical phantoms to evaluate the feasibility of the method, an IRB approved initial investigation was performed using temporally acquired DBT images of human subjects. Simulated subtle masses were used to provide the known temporal changes and ROI alignment was performed after volumetrically warping one of the datasets using corresponding location markers such as calcifications, vessel bifurcations, and breast edges. The results showed that structural discrepancies, due to differences in positioning and compression between temporally spaced acquisitions, caused slight anatomical variations between reconstructed slices that significantly reduced registration accuracy and subtraction. The misalignment of the datasets increased the contrast in the subtraction image and did not increase lesion conspicuity. Although, the feasibility of combining the two methods using simulation and physical phantoms may have shown to be promising, qualitative analysis of the results using actual human subject data did not indicate a significant improvement in breast cancer detection.

These results prompted the change in scope of the project to focus on developing a realistic computerized breast phantom (RCBP) to be used for breast imaging research. The RCBP can be used for simulations that study the imaging system design, acquisition protocols, reconstruction algorithms, and image processing techniques. The RCBP is an inexpensive option compared to physical phantoms and can be modified in terms of size and tissue distribution to provide a “known truth” for a variety of breasts. One goal of RCBP development is to use dedicated breast CT data as the foundation for the phantom and have the ability to create different realizations of breast morphology based on actual patient data. The phantom developed in this project will provide a vital tool to investigate current and emerging breast imaging methods and techniques with the ability to simulate realistic, predictive patient imaging data.

Body

Task 1. To generate tomosynthesis datasets of simulated and physical breast phantom.

1a. Develop a realistic computer simulated breast phantom simulation and generate up to 50 simulated tomosynthesis projection data with the phantom undergoing simulated tissue deformation: In progress

As reported in the last summary, this task became the focus of the project. The computerized breast phantom developed in this work will improve on existing, simpler phantoms by being both anatomically realistic and detailed. In addition, it will provide an optimization tool for breast imaging research by accounting for the effect of anatomy and its variations in a population. Since the last summary, several improvements have been made to the RCBP¹.

In addition to denoising the dedicated breast CT dataset with an algorithm developed in our lab, a post-reconstruction scatter correction algorithm was used to correct for background non-uniformity in each axial image². The cupping artifact was modeled as a circularly symmetric additive background signal profile in the

reconstructed image set. The scatter artifact lowers the true tissue signal in a non-uniform way with a greater bias towards the breast center. The correction signal is based on a sampling technique to obtain an estimate of the adipose tissue signal in the axial images. The simulated cupping artifact (Figure 1) was subtracted from the breast volume in order to correct for scatter.

Additional segmentation methods were implemented to further improve the high resolution detail available in the phantom. Breast volume masking was followed by an iterative histogram classification to provide initial tissue segmentation. Next, morphological techniques were used to include joining elements that did not appear in the initial segmentation. Finally, the fibroglandular tissue was segmented to include the innate marbling effect of fibroglandular and adipose tissue. These methods are more completely described in Appendix 2. The resulting segmentation (Figure 2) more closely resembles the original breast data than previous segmentation results.

The next step in the process was to create the computerized compressible breast model from the segmented data (Figure 3). Currently, a simplistic compression model is used, which does not take into consideration the varying mechanical properties of the different breast tissue. A finite element model (FEM) of the breast is necessary to create a realistic compression model of the breast. In order to use finite element methods, a volumetric mesh needs to be generated. The first step to create the FEM of the breast was creating a mesh surface model using the Matlab *isosurface* function, which renders a polygon surface mesh in volumetric data. The surface model includes all of the intricate tissue connections within the breast; however, it lacks the volumetric information necessary for an FEM of the breast. In order to accomplish creating the FEM, a pre-processing tool is used to generate the volumetric mesh from the surface mesh.

The high resolution of the breast data creates a very complex nodal structure. Typically, pre-processing tools can handle on the order of 5 thousand nodes; unfortunately the breast model has over 5 million nodes (Figure 4). This complicated the meshing considerably, and in order to work, the model has to be down-sampled, which reduces the complexity of the resulting compressed model. Currently the full resolution volumetrically meshed breast has yet to be generated, although a lower resolution volumetric mesh is possible. Although this detracts from the high-resolution of the current model, this will demonstrate the method that can generate a high resolution, compressible breast model when future iterations of pre-processing software are able to handle more complex data.

Issues and future work: Ultimately the goal of this RCBP effort is to create a database of anatomically realistic computerized breasts that are based on real data and used in breast imaging research. The computational anatomy algorithm that will be used to morph between breast data in order to generate any configuration of breast tissue density and morphology still needs to be created and will be completed during the course of the investigators dissertation. The current compression model is too simplistic and an FEM compression model of the breast still needs to be created as this is a necessary piece of the model for imaging research in methods that use compression. In order to create the FEM model, the volumetric mesh step requires a down sampling of the data's resolution. Although, resulting in a coarser resolution, these methods demonstrate how a high-resolution RCBP may be generated in the future when pre-processing software can process this complicated structure.

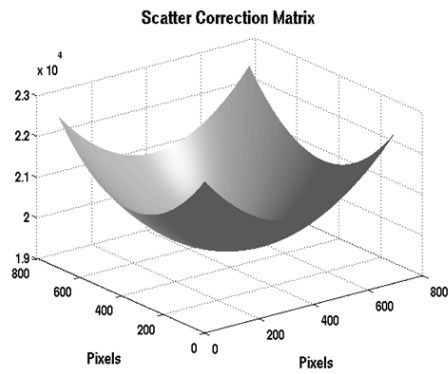


Figure 1: Scatter correction matrix subtracted from each axial slice to correct for background non-uniformity.

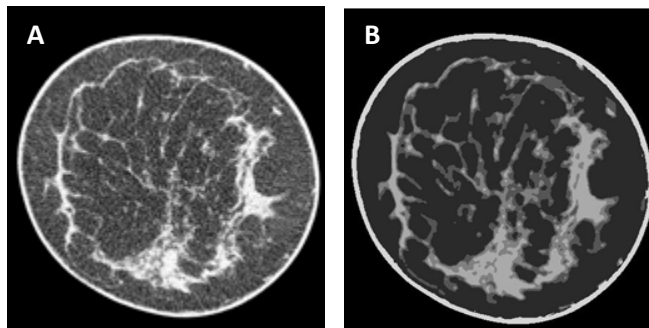


Figure 2: (A) original CT data. (B) Segmented CT data.

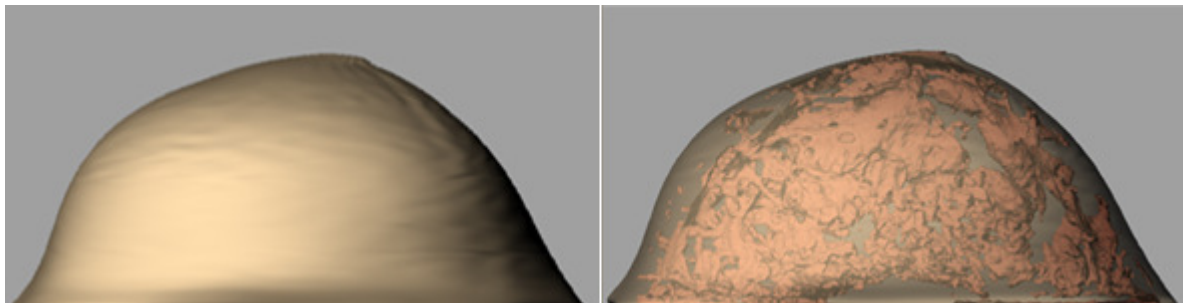


Figure 3: Surface model of the breast skin and fibroglandular tissue.

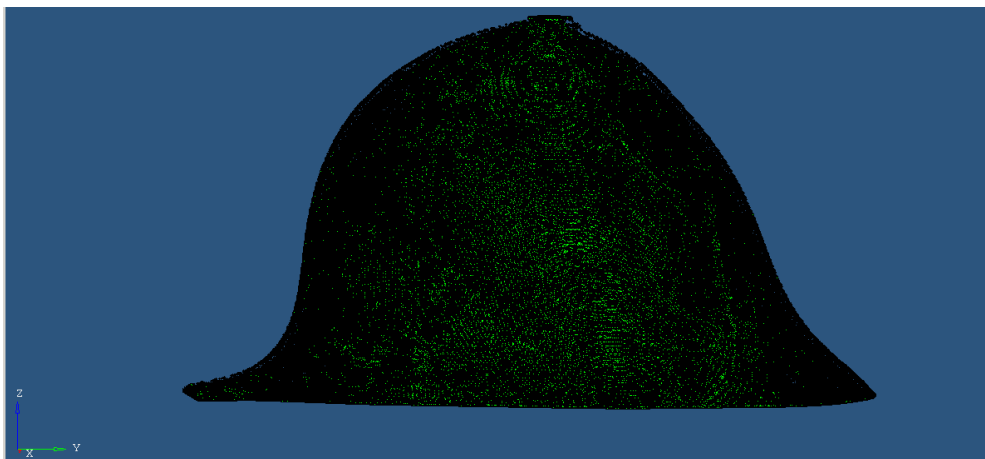


Figure 4: Screen shot of breast surface mesh in pre-processing software.

Simulated mammogram acquisition can be performed directly on the mesh surface model. An example of how the breast phantom can be changed to generate different breast morphology is demonstrated in Figure 5. This shows two representations of the same breast taken with slightly different attenuation coefficient values used to define the fibroglandular tissue. Tomosynthesis data can also be acquired of the breast phantom, as previously reported.

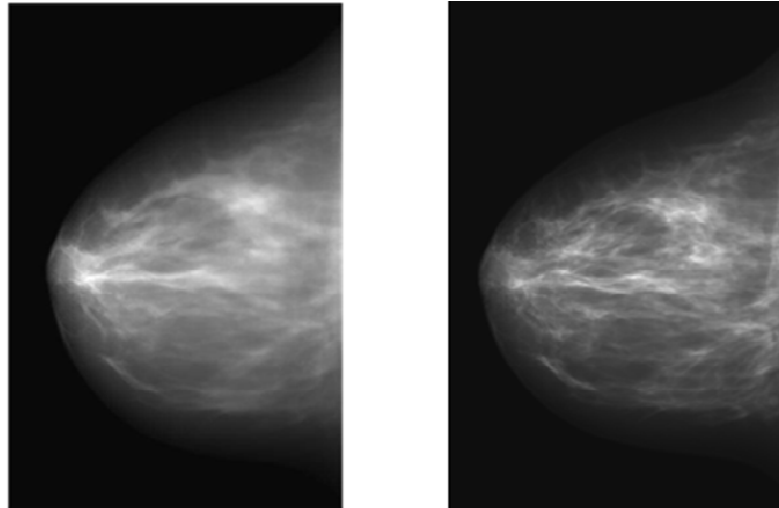


Figure 5: Simulated mammograms of the same breast phantom to demonstrate user defined changes in breast morphology.

1b. Acquire up to 30 tomosynthesis projections of a compressible and deformable physical phantom with physically simulated anatomy and under different simulated temporal discrepancies: Complete

Previously, the investigator showed that it was feasible to acquire tomosynthesis projections of a compressible and deformable physical phantom. Inside of the breast phantom the investigator inserted a number of objects to simulate breast parenchyma. The investigator took multiple tomosynthesis exams of a compressed breast rotated in-between image acquisitions. There were three scans taken in total: one in the original orientation and original number of simulated lesions; the second with the breast slightly rotated with the original number of simulated lesions; and the third with the breast rotated in a different way and without some of the simulated lesions. Unfortunately, the materials used for the physical phantom were not ideal and the tomosynthesis images reconstructed from the acquisition do not look realistic enough to use for the observer study. After investigation using human subject data showed that temporal subtraction of DBT images did not greatly improve the detectability of malignant morphology, effort towards this task was ended to focus on task 1a.

1c. Utilize up to 3 different tomosynthesis reconstruction algorithms (Filtered Back Projection, Matrix Inversion Tomosynthesis, and Gaussian Frequency Blending) to create tomosynthesis data sets of the simulated and physical phantom: Complete

As reported previously the DBT images were reconstructed using the Filtered Back Projection algorithm. However, the images did not appear to realistically resemble actual breast tomosynthesis images from human subjects. Work on this task was halted when the temporal subtraction of human subject DBT images did not improve lesion conspicuity and the focus of the project was put towards Task 1a.

Task2. To develop a registration and subtraction algorithm: Complete

As reported in the last summary, the investigator received IRB approval to use temporally acquired breast tomosynthesis datasets of two human patients. An algorithm was developed to register and subtract two clinical breast tomosynthesis datasets of the same patient that were acquired under IRB protocol with nine months temporal spacing. Calcification points common in the two image sets were used to manually determine 3D angular rotations and translations of the breast that occurred between acquisitions. One image set was rigidly transformed to better align the two image sets. A registration method developed by Althof et al. was implemented to align and subtract ROIs in the two image sets using cross correlation³. One image's ROIs could be matched with any ROI in the other image set within a certain volume of data. This was done in an attempt to limit the area of registration to a region that was most likely to contain the corresponding match. Angular rotations of the ROI $\pm 15^\circ$ were also explored in order to match the ROIs more effectively. In addition, a subtle round mass was simulated in the images to highlight both known and significant temporal change between acquisitions. To minimize potential mis-registration, the algorithm was run twice to find the best ROI to subtract and then again, to subtract the ROI with the simulated lesion from its best matched ROI. Refinement of the algorithm was not pursued after the simple subtraction did not yield improvements in lesion detection.

Task3. To evaluate the temporal subtraction method on the images: Complete

As previously reported, although constraints were implemented to disregard registering to image noise, there were too many inter-image variations to adequately align the breast ROIs properly. If the overarching image gradients matched, there were still shading differences that appeared to increase the subtracted image contrast rather than decreasing it as expected. In addition, there were many ROIs that did not adequately match up with a corresponding ROI. An overwhelming number of ROIs adequately registered, however they were incorrect matchings in inappropriate locations and reflected a failure of the matching algorithm. These ROIs further increased image contrast because of incorrect registration issues. Some ROIs appeared to have subtracted similar breast texture; however these were still not perfectly aligned and created increased contrast in the subtraction. The addition of a simulated subtle mass was not visible in the resulting subtraction. This method did not show any increase in lesion conspicuity, most likely due to the overwhelming amount of mis-registered ROIs and severely dissimilar registered ROIs. The major complication for the registration algorithm was most likely due to differences in positioning and compression forces used during the temporally spaced acquisitions. This caused structural discrepancies that created slight anatomical variations between reconstructed slices to significantly reduce registration ability and subtraction. The non-isotropic resolution of the imaging data did not allow for in-between plane information to be factored into the mechanical transformation algorithm. This contributed to mis-registration issues since information between planes, did not get transferred onto a plane, and was not available for registration. These results prompted the investigator to focus solely on creating a realistic computerized breast phantom.

Task 4. To concurrently complete other aspects of training program: In progress

The investigator has attended several conferences over the course of the award period, including: SPIE medical imaging conference, DOD BCRP Era of Hope Award, and BRIC GE symposium on Breast Imaging. The investigator has published several first author papers, including one peer-reviewed article in Medical Physics. In addition, the investigator has been a co-author on several papers during the course of the DOD award.

Key Research Accomplishments

- Dedicated breast CT data of human subjects was processed for basis of realistic computerized breast phantom
- Scatter correction algorithm was implemented to correct for background non-uniformity
- A refined automated segmentation algorithm was developed
- A mesh-surface model of a single breast was created with all tissues
- Pre-processing software to complete volumetric mesh was chosen (Altair Hyperworks)
- Simulated mammographic and tomosynthesis data was acquired
- Compression algorithm should be made more realistic using finite-element methods
- An algorithm for the temporal subtraction for digital breast tomosynthesis human datasets was developed and implemented
- Results from human data shows that temporal subtraction of digital breast tomosynthesis data may be infeasible.

Reportable Outcomes

1. **C. M. Li** and J. T. Dobbins, III, "Methodology for Determining Dose Reduction for Chest Tomosynthesis," SPIE Medical Imaging 2007: Physics of Medical Imaging 6510, (2007).
2. **C. M. Li**, W. P. Segars, J. Y. Lo, et al., "Three-dimensional computer generated breast phantom based on empirical data," Medical Imaging 2008: Physics of Medical Imaging **6913**, 691314 (2008).
3. Oral presentation SPIE Medical Imaging 2008.
4. McAdams H.P., Dobbins J.T., III, **Li C.M.**, "Digital Tomosynthesis of the Chest for Lung Nodule Detection: Initial Clinical Experience," RSNA 93rd Scientific Program (2007).
5. Dobbins J.T., III, McAdams H.P., Godfrey D.J., **Li C.M.**, "Digital Tomosynthesis of the Chest," Journal of Thoracic Imaging 23, 86-92, (2008).
6. Dobbins, J. T., III, McAdams, Song J., **Li C.M.**, Godfrey D.J., DeLong D.M., Paik S., Martinez-Jimenez, S., "Digital tomosynthesis of the chest for lung nodule detection: Interim sensitivity results from an ongoing NIH-sponsored trial," Medical Physics 35, 2554-2557, (2008).
7. Preliminary exam completed.
8. **C. M. Li**, W. P. Segars, G. D. Tourassi, J. M. Boone, J. T. Dobbins, III, "Methodology for generating a 3D computerized breast phantom from empirical data," Medical Physics 36, 3122-3131 (2009).
9. **C. M. Li**, W. P. Segars, J. Y. Lo, A. I. Veress, J. M. Boone and J. T. D. III, "Computerized 3D breast phantom with enhanced high-resolution detail," Medical Imaging 2009: Physics of Medical Imaging, Orlando, FL, (2009).
10. Oral presentation SPIE Medical Imaging 2009.
11. 2nd author for an abstract accepted for SPIE Medical Imaging 2010. "*In vivo* characterization of breast tissues through absolute attenuation coefficients using dedicated cone-beam CT."
12. NIH NCI grant 1R01CA134658 "3D Digital Breast Phantoms For Multimodality Research" was funded based on the RCBP developed during this project.

Conclusions

An algorithm to implement the original goal for the project, developing a temporal subtraction algorithm for tomosynthesis data, was attempted on actual human data. The initial results from this effort showed that the combination of the two methods did not increase lesion detectability and resulted in many subtraction artifacts. The artifacts are believed to be primarily due to differences in patient positioning, compression amounts, and hormonal fluctuations in breast composition. In the future, investigation into the temporal subtraction technique may be warranted with fully 3D imaging data as the non-isotropic resolution of the data did not allow for in-between plane information to be factored into image registration. The investigator decided to change the focus of the project toward developing a computerized breast phantom.

This project will present researches with a realistic breast phantom that is based on actual human data and offers a number of unique properties not currently available in other phantoms. This will provide a realistic breast phantom that includes the ability to simulate of a variety of sizes, compositions, and deformations. The investigator has already received several requests to use the phantom for research, although none have been granted as the phantom is not yet ready for public release. This project has the potential to contribute significantly to breast imaging research for the advancements of detection techniques and technologies.

References

1. C. M. Li, W. P. Segars, G. D. Tourassi, J. M. Boone, J. T. Dobbins, III, "Methodology for generating a 3D computerized breast phantom from empirical data," *Medical Physics* 36, 3122-3131 (2009).
2. M. C. Altunbas, C. C. Shaw, L. Chen, C. Lai, X. Liu, T. Han and T. Wang, "A post-reconstruction method to correct cupping artifacts in cone beam breast computed tomography," *Medical Physics* 34, 3109-3118 (2007).
3. R. J. Althof, M. G. J. Wind and J. T. Dobbins, III, "A rapid and automatic image registration algorithm with subpixel accuracy," *IEEE Trans Med Imag* 16, 308-316 (1997).

Appendix

1. C. M. Li, W. P. Segars, J. Y. Lo, et al., "Computerized 3D breast phantom with enhanced high resolution detail," *Medical Imaging 2008: Physics of Medical Imaging* 7258, (2009).
2. C. M. Li, W. P. Segars, G. D. Tourassi, J. M. Boone, J. T. Dobbins, III, "Methodology for generating a 3D computerized breast phantom from empirical data," *Medical Physics* 36, 3122-3131 (2009).
3. P. Madhav, C.M. Li, O.I. Christianson, M.P. Tornai, "*In vivo* characterization of breast tissues through absolute attenuation coefficients using dedicated cone-beam CT," *Medical Imaging 2010: Physics of Medical Imaging* (2010), submitted abstract.

Computerized 3D Breast Phantom with Enhanced High-Resolution Detail

Christina M. Li^{1,2}, W. Paul Segars^{1,2,3,4}, Joseph Y. Lo^{1,2,3,4}, Alexander I. Veress⁵,
John M. Boone⁶, James T. Dobbins III^{1,2,3,4}

¹Department of Biomedical Engineering, Duke University, Durham, NC

²Carl E. Ravin Advanced Imaging Laboratories, Duke University Medical Center, Durham, NC

³Department of Radiology, Duke University Medical Center, Durham, NC

⁴Medical Physics Graduate Program, Duke University, Durham, NC

⁵Mechanical Engineering Department, University of Washington, Seattle, WA

⁶Department of Radiology, X-ray Imaging Laboratory, University of California, Davis Medical Center, Sacramento, CA

ABSTRACT

We previously proposed a three-dimensional computerized breast phantom that combines empirical data with the flexibility of mathematical models¹. The goal of this project is to enhance the breast phantom to include a more detailed anatomy than currently visible and create additional phantoms from different breast CT data. To improve the level of detail in our existing segmentations, the breast CT data is reconstructed at a higher resolution and additional image processing techniques are used to correct for noise and scatter in the image data. A refined segmentation algorithm is used that incorporates more detail than previously defined. To further enhance high-resolution detail, mathematical models, implementing branching algorithms to extend the glandular tissue throughout the breast and to define Cooper's ligaments, are under investigation. We perform the simulation of mammography and tomosynthesis using an analytical projection algorithm that can be applied directly to the mathematical model of the breast without voxelization². This method speeds up image acquisition, reduces voxelization artifacts, and produces higher resolution images than the previously used method. The realistic 3D computerized breast phantom will ultimately be incorporated into the 4D-XCAT phantom³⁻⁵ to be used for breast imaging research.

Keywords: Imaging of the breast (MG), Phantoms (PHT), Simulation (SIM)

Introduction

Breast imaging has been instrumental in reducing the mortality of breast cancer by allowing for earlier detection and better quantification of the disease⁶. Further improvements to breast imaging techniques and systems allow for improved patient care and outcomes. Computer phantoms are increasingly used in medical imaging research and development because they can be modified in terms of size and tissue distribution, provide a "known truth" to aid in evaluating imaging devices and techniques, and do not require any additional material costs or production time other than software processing. Several computerized breast phantoms were created for breast imaging using two distinct methods⁷⁻¹⁵: mathematically based models defined by geometric primitives and voxelized models derived from real human-subject data. The major limitation of mathematically based models is that they lack realism due to their simplistic shape definitions for breast tissue. Although more realistic, voxelized models are limited by both their anatomically fixed nature and the limited number of available breast definitions. The computerized three-dimensional (3D) breast phantoms discussed in this work are unique because they are created from the combination of mathematical models and empirical data, which results in realistic and flexible phantoms that can be modified in terms of size and tissue distribution. This project is to enhance the current breast phantom to include high-resolution detail that is not currently available in the previous version. Information from these computerized breast phantoms will ultimately be incorporated into the widely-distributed four-dimensional (4D) extended non-uniform rational b-splines (NURBS) based Cardiac-Torso (XCAT) phantom developed by Segars *et al.* to be used for breast imaging research²⁻⁵.

Methods

Image Processing

Each breast phantom is based on data collected with a prototype dedicated breast CT scanner at UC Davis¹⁶⁻¹⁹. During acquisition, each breast is scanned separately and the mean glandular radiation dose delivered to the breast was constrained to be the same as two-view mammography. The low-dose acquisition of the breast data as well as the cone-beam geometry of the CT system resulted in image degradation due to scatter radiation and quantum noise. Correction of scatter and noise is a necessary part of this project because the non-uniformity of the background may cause the glandular tissue values to be lower than the adipose tissue values and vice versa. This becomes a problem when we need to segment the breast CT data by using value based techniques in order to create the breast model. Without adequate scatter and noise correction, the segmentation algorithm will not accurately distinguish between different types of tissue.

A denoising algorithm was developed by Xia *et al.* in order to perform noise correction on breast CT projection images prior to reconstruction and without loss of spatial resolution²⁰. The CT projection images were processed with 40 iterations of the denoising algorithm and were reconstructed using a custom written filtered back-projection algorithm. The resulting dataset had axial slices with an in-plane resolution of 250 μm and slice spacing of 500 μm . An algorithm similar to the post-reconstruction scatter correction method developed by Altunbas *et al.* was used to correct for the background non-uniformity in each axial image due to scatter²¹.

Segmentation

After noise and scatter correction, the next step is the classification of the CT data into the various breast tissues, which will define the appropriate physical characteristics of each voxel during simulated compression and image acquisition. An automated segmentation algorithm was developed to segment the skin, glandular, and adipose tissues. Several steps were used to segment the breast data. We used a histogram technique to provide the general basis for segmentation of the glandular tissue. This technique was similar to the technique used by Packard and Boone²² and was used to define a threshold for each slice.

Morphologically based steps were used to further refine the segmentation as well as regain glandular tissue that was not classified with the histogram segmentation. Slices were examined for ellipsoid shaped fragments of glandular tissue and a search area around the glandular island was examined for potentially disjointed segments. The joining section between the two glandular segments, previously unidentified as glandular tissue, was labeled as glandular with this ellipsoidal connection method. In addition, a method was developed to search for patterns of distances between large glandular fragments and join the two fragments together if they were located close enough.

After the glandular tissue had been segmented, a further classification of the glandular tissue was performed based on density. Marbling of breast tissue results in different ratios of fat interspersed with glandular tissue and vice versa, therefore the segmented glandular tissue was divided into three different levels of density. This served to give the glandular tissue a more realistic representation of the breast than a single density level.

Model Creation

Computer graphics techniques were used to generate a 3D mesh surface model of the breast from the segmented data. In the mesh model, triangles were used to estimate the curved surfaces of the tissue. Once

the mesh model was created, additional operations may be performed to manipulate or deform the mesh. The resulting polygon mesh of each tissue was input to the Rhinoceros NURBS modeling software²³ and a surface was fit to it in order to display the breast model.

Compression of the Breast Phantom

The breast is compressed during mammography and this is essential to produce high quality images. It is necessary to create a compression model component in order to make the breast phantom applicable for research in breast imaging. For this preliminary work we used a simplistic compression model that did not account for the mechanical properties of different tissues presented previously¹. The breast was assumed to be incompressible and isotropic and the model simulated compression between stiff plates.

Simulated Mammogram Acquisition

The objective of all imaging phantoms is to generate realistic images that accurately model the imaging process. Therefore, simulated image acquisition is a necessary component to evaluate the phantom's clinical utility. Previously, voxelized data was interpolated from the mesh breast model and then used for simulated acquisition. This process was computationally intensive and required a reduction in the models complexity, which resulted in voxelization errors and decreased resolution in the simulated images. In this work, the images were generated with an analytical projection algorithm that models the x-ray imaging process and includes effects from quantum noise⁴. The program has the ability to simulate parallel, fan, or cone-beam geometries directly from the compressed mesh surface definition using a given polychromatic x-ray spectrum²⁴. We simulated mammograms with geometry similar to the Siemens Mammomat Novation System^{TOMO} (SID – 653.2 cm and air gap –15 mm) at 30 kVp. Material characteristics of the breast phantom were defined using a report from the International Commission on Radiation Units. The different density levels of glandular tissue were assigned attenuation coefficients equally distributed between fat and muscle, skin tissue was assigned the same attenuation coefficient as muscle, and adipose was assigned fat²⁵.

MultiModality Applications

The phantom has applications beyond simulated mammograms and can be used by many other modalities as well. To demonstrate the phantom's abilities, tomosynthesis, MRI, and ultrasound images were simulated of the breast phantom. The tomosynthesis projection images were simulated in a similar method to the mammogram images using the Siemens Mammomat Novation System. Twenty-five projection images were acquired over a 50° arc and reconstructed using Siemens' proprietary reconstruction algorithm^{26, 27}. MRI data was simulated from the phantom using ODIN²⁸. The T1, T2, and spin density properties of the breast structures were derived based on experimental studies²⁹. Ultrasound data was simulated using Field II³⁰ setting the acoustical properties of the tissues according to Madsen, et al³¹.

Results

Segmentation

The increased number of denoising iterations and addition of scatter correction contributed to an improved segmentation of the reconstructed datasets in the central breast area over the previous segmentation. In addition the additional segmentation steps increased the high-resolution detail of the phantom. The density differentiation of the segmented glandular tissue also served to more realistically represent the marbling effect of adipose and glandular tissue in the breast (Figure 1).

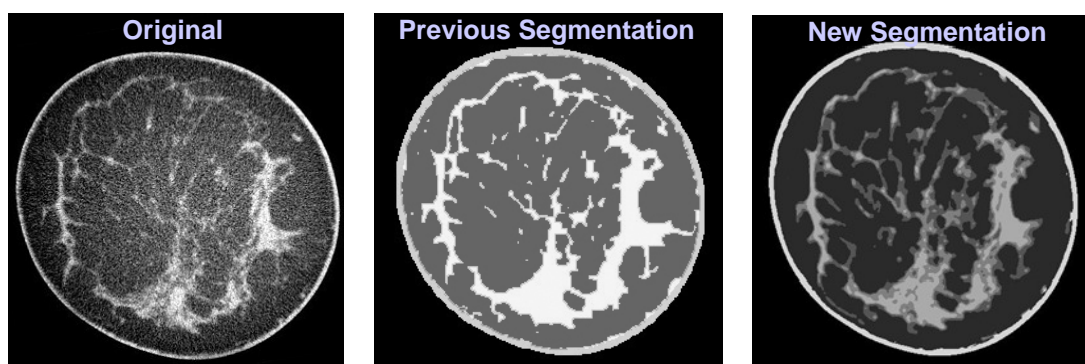


Figure 1: a) Original data prior to image processing. b) Previous segmentation. c) New segmentation with improved segmentation additional image processing.

Model

A new model was generated from the segmented data and is shown in Figure 2.

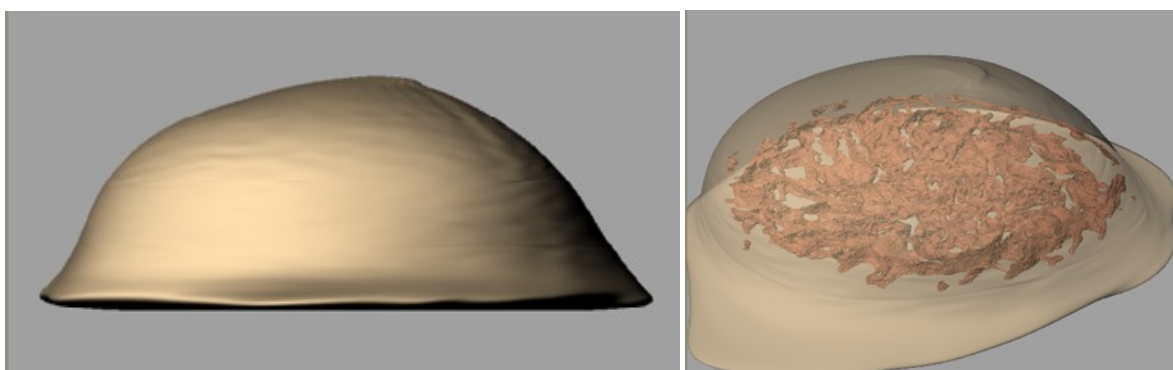


Figure 2: Surface rendering of the skin is shown on the left and an illustration of the inner structures is on the right.

Simulation of a Projection Mammogram

The previous simulated image acquisition method to generate a simulated projection mammogram required time consuming and computationally intensive voxelization of the phantom and resulted in a reduced resolution from 400 μm to 800 μm in the final image. The new analytical projection algorithm used in this work required seconds to run and resulted in 250 μm resolution in the final image. The image was processed with a sigmoidal function in order to display the image optimally (Figure 3a).

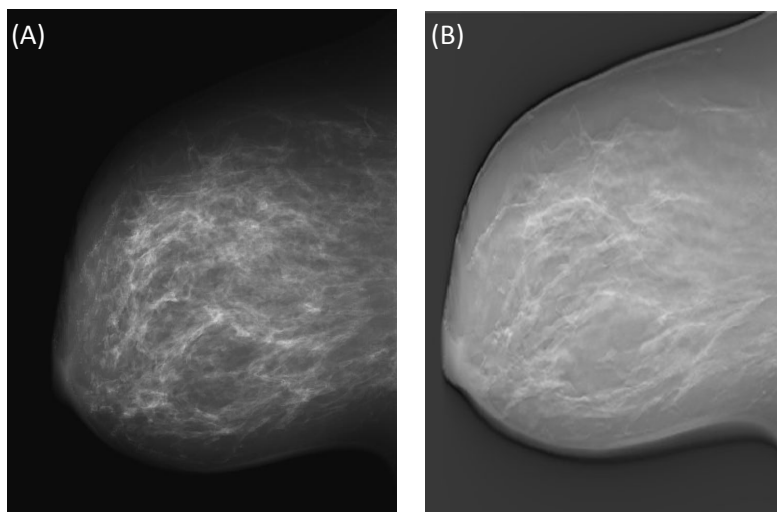


Figure 3: a) Simulated mammogram of a compressed breast phantom with improved high resolution detail using analytical projection algorithm. b) Simulated Tomosynthesis slice of the phantom

Multimodality Applications

A tomosynthesis reconstructed image is shown in Figure 3b. Figure 4 displays a comparison of real breast MRI data on the left and simulated breast MRI of the phantom on the right. The images were not acquired of the same human subject.

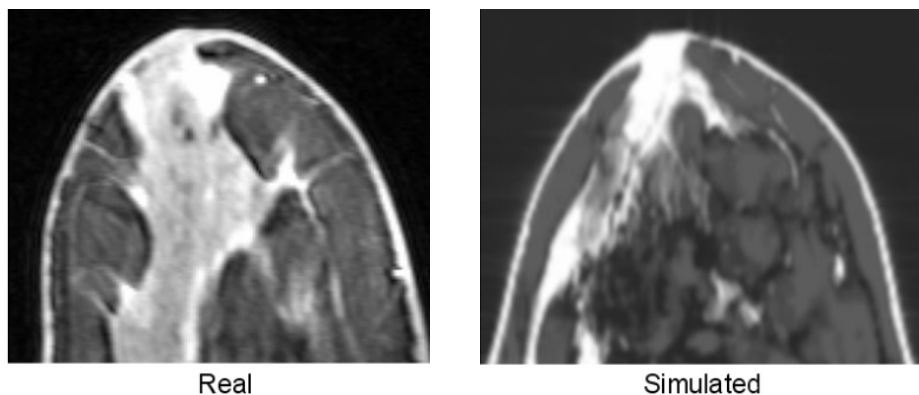


Figure 4: MRI of a real breast compared to a simulated MRI of the phantom.

Figure 5 displays a comparison of real breast ultrasound data on the left and simulated ultrasound of the phantom on the right. The human subject data was not acquired

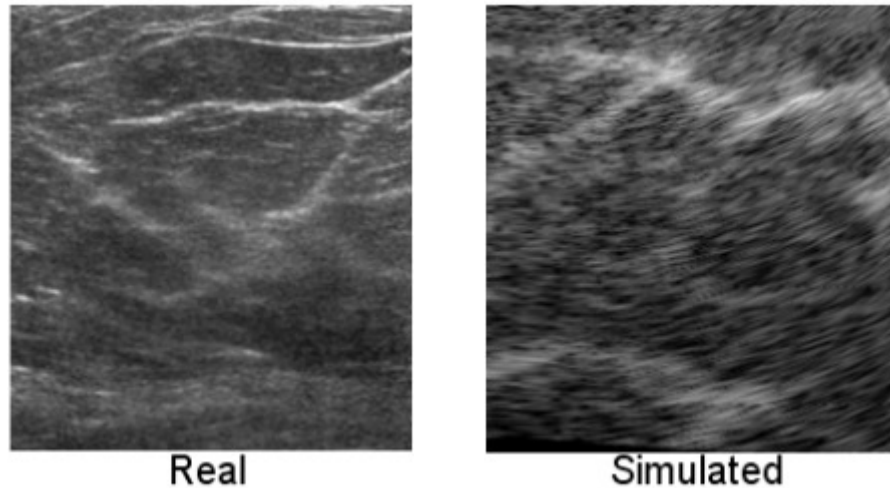


Figure 5: Ultrasound of a real breast compared to a simulated Ultrasound of the phantom.

Future Work

Modeling of additional structures

In theory, the segmentation should be able to produce a model at approximately the same resolution as the CT data upon which it is based. If the segmentation does not result in a phantom with acceptable resolution, we will investigate combining our segmentation with mathematical formulations. Mathematical branching algorithms are under investigation to extend the breast ductal network and enhance and replace the missing high resolution detail for more realistic and complete breast tissue modeling. We previously developed such methods to define complete models for the airway tree in the lungs and the coronary arteries of the heart^{32, 33}. These branching methods used segmented data for the initial basis of the airway and coronary trees and then used a physiologically-based mathematical algorithm to further propagate the trees to complete them. We also plan to add further detail by defining the Cooper's ligaments using geometrical NURBS surfaces.

Realistic Compression using Finite Element Methods

The current simplistic compression method used currently does not realistically simulate breast compression. The interaction between adjoining tissues and their different mechanical characteristics were not taken into account and this affects the tissue distribution in the resulting images. Finite-element methods that take into account different material properties of the breast tissue will be used to realistically model breast compression. A finite element mesh will be based on the segmented breast data, which will also be used to define the mechanical properties for a realistic breast compression model. Boundary conditions will be defined and breast compression will be simulated between flat plates as demonstrated in Figure 6.

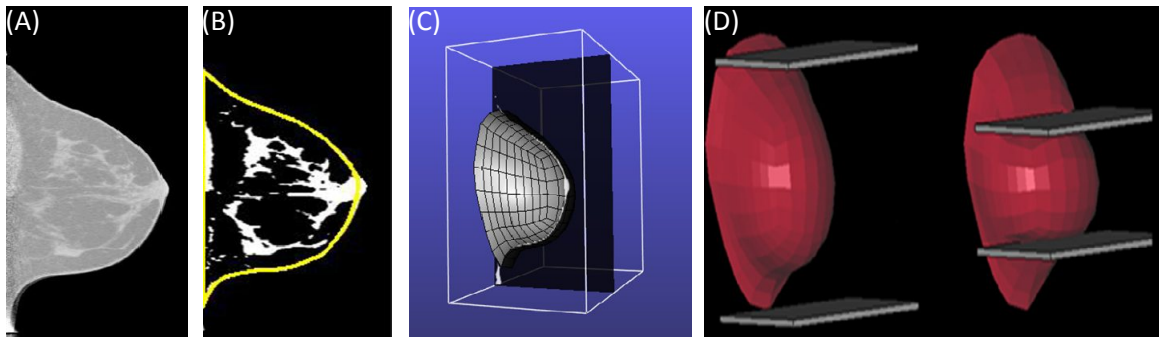


Figure 6: (A) Slice of CT data; (B) Segmented data; (C) Finite element mesh model; (D) Compression model.

Conclusions

This work will further enhance the breast phantom to include finer detailed structures that are not currently visible and generate additional phantoms from different breast CT data. These computerized breast phantoms will ultimately be incorporated into the 4D-XCAT phantom in order to make it applicable to breast imaging research.

Acknowledgements

We would like to thank Dr. Mertelmeier at Siemens AG Medical Solutions for the use of the FBP software. This work has been supported by the Department of Defense Breast Cancer Research Program (W81XWH-06-1-0732) and National Institutes of Health (NIH) (R01EB001838), NIH/NCI (R01CA112437), NIH/NCI (R01CA94236).

References

- [1]C. M. Li, W. P. Segars, J. Y. Lo, et al., "Three-dimensional computer generated breast phantom based on empirical data," *Medical Imaging 2008: Physics of Medical Imaging* **6913**, 691314 (2008).
- [2]W. P. Segars, M. Mahesh, T. J. Beck, E. C. Frey and B. M. W. Tsui, "Realistic CT simulation using the 4D XCAT phantom," *Medical Physics* **35**, 3800-3808 (2008).
- [3]W. P. Segars, "Development and application of the new dynamic NURBS-based cardiac-torso (NCAT) phantom," *Journal* (2001).
- [4]W. P. Segars, M. Mahesh, T. Beck, E. C. Frey and B. M. W. Tsui, "Validation of the 4D NCAT simulation tools for use in high-resolution x-ray CT research," *SPIE Medical Imaging Conference* **5745**, 828-834 (2005).
- [5]W. P. Segars, B. M. W. Tsui, E. C. Frey and E. K. Fishman, "Extension of the 4D NCAT phantom to dynamic x-ray CT simulation," *IEEE Nuclear Science Symposium* **5**, 3195-3199 (2003).
- [6]ACS, "American Cancer Society: Cancer Facts and Figures 2008. Atlanta, Ga: American Cancer Society 2008.," (2008).
- [7]K. Bliznakova, Z. Bliznakov, V. Bravou, Z. Kolitsi and N. Pallikarakis, "A three-dimensional breast software phantom for mammography simulation," *Physics in Medicine and Biology* **48**, 3699-3719 (2003).
- [8]C. Zyganitidis, K. Bliznakova and N. Pallikarakis, "A novel simulation algorithm for soft tissue compression," *Medical and Biological Engineering and Computing* **Online First**, (2007).
- [9]P. Bakic, M. Albert, D. Brzakovic and A. Maidment, "Mammogram synthesis using a three-dimensional simulation. III. Modeling and evaluation of the breast ductal network," *Med Phys* **30**, 1914-1925 (2003).

- [10]P. Bakic, M. Albert, D. Brzakovic and A. Maidment, "Mammogram synthesis using a 3D simulation. II. Evaluation of synthetic mammogram texture," *Medical Physics* **29**, 2140-2151 (2002).
- [11]P. Bakic, M. Albert, D. Brzakovic and A. Maidment, "Mammogram synthesis using a 3D simulation. I. Breast tissue model and image acquisition simulation," *Medical Physics* **29**, 2131-2139 (2002).
- [12]J. Zhou, B. Zhao and W. Zhao, "A Computer simulation platform for the optimization of a breast tomosynthesis system," *Medical Physics* **34**, 1098-1109 (2007).
- [13]J. Shorey, "Stochastic Simulations for the Detection of Objects in Three Dimensional Volumes: Applications in Medical Imaging and Ocean Acoustics," *Journal PhD*, 257 (2007).
- [14]C. Hoeschen, U. Fill, M. Zankl, et al., "A High-Resolution Voxel Phantom of the Breast for Dose Calculations in Mammography," *Radiation Protection Dosimetry* **114**, 406-409 (2005).
- [15]L. Zhou, J. Oldan, P. Fisher and G. Gindi, "Low-Contrast Lesion Detection in Tomosynthetic Breast Imaging Using a Realistic Breast Phantom," *SPIE Medical Imaging: Physics of Medical Imaging* **6142**, (2006).
- [16]K. K. Lindfors, J. M. Boone, T. R. Nelson, et al., "Dedicated Breast CT: Initial Clinical Experience," *Radiology* **246**, 725-733 (2008).
- [17]J. M. Boone, T. R. Nelson, K. K. Lindfors and J. A. Seibert, "Dedicated Breast CT: Radiation Dose and Image Quality Evaluation," *Radiology* **221**, 657-667 (2001).
- [18]J. M. Boone, A. L. C. Kwan, T. R. Nelson, et al., "Performance assessment of a pendant-geometry CT scanner for breast cancer detection," *2005 Proc. SPIE: Phys. of Med. Imag.* **5745**, 319-323 (2005).
- [19]J. M. Boone, A. L. Kwan, K. Yang, et al., "Computed tomography for imaging the breast," *Journal of Mammary Gland Biology and Neoplasia* **11**, 103-111 (2006).
- [20]J. Xia, J. Lo, K. Yang, C. E. Floyd and J. Boone, "Dedicated breast computed tomography: Volume image denoising via a partial-diffusion equation based technique " *Medical Physics* **35**, 1950-1958 (2008).
- [21]M. C. Altunbas, C. C. Shaw, L. Chen, et al., "A post-reconstruction method to correct cupping artifacts in cone beam breast computed tomography," *Medical Physics* **34**, 3109-3118 (2007).
- [22]N. Packard and J. M. Boone, "Glandular segmentation of cone beam breast CT volume images," *Medical Imaging 2007: Physics of Medical Imaging* **6510**, (2007).
- [23]"Rhinceros," <http://www.rhino3d.com/>,
- [24]J. M. Boone, "Normalized glandular dose (DgN) coefficients for arbitrary x-ray spectra in mammography: Computer-fit values of Monte Carlo derived data," *Medical Physics* **29**, 869-875 (2002).
- [25]U. S. Natl. Bur. Stand, *Report of the task group on reference man: Anatomical values for reference man*, (1975).
- [26]J. Ludwig, T. Mertelmeier, H. Kunze and W. Haerer, "A Novel Approach for Filtered Backprojection in Tomosynthesis Based on Filter Kernels Determined by Iterative Reconstruction Techniques," *9th international workshop on Digital Mammography* **5116**, 612-620 (2008).
- [27]T. Mertelmeier, J. Orman, W. Haerer and M. K. Dudam, "Optimizing filtered backprojection reconstruction for a breast tomosynthesis prototype device," *SPIE Medical Imaging: Physics of Medical Imaging* **6142**, (2006).
- [28]T. H. Jochimsen and M. von Mengershausen, "Object-oriented development interface for NMR," *Journal of Magnetic Resonance* **170**, 67-78 (2004).
- [29]S. J. Graham, S. Ness, B. S. Hamilton and M. J. Bronskill, "Magnetic Resonance Properties of Ex Vivo Breast Tissue at 1.5 T," *Magnetic Resonance in Medicine* **38**, 669-677 (1997).
- [30]J. A. Jensen, "A Model for the Propagation and Scattering of Ultrasound in Tissue," *J.Acoust.Soc.Am* **89**, 182-191 (1991).
- [31]E. L. Madsen, W. A. Berg, E. B. Mendelson and G. R. Frank, "Anthropomorphic Breast Phantoms for Qualification of Investigators for ACRIN Protocol 6666," *Radiology* **239**, 869-874 (2006).
- [32]J. Garrity, W. P. Segars, S. B. Knisley and B. M. W. Tsui, "Development of a dynamic model for the lung lobes and airway tree in the NCAT phantom," *IEEE Transactions on Nuclear Science* **50**, 378-383 (2003).
- [33]G. S. K. Fung, W. P. Segars, K. Taguchi, E. K. Fishman and B. M. W. Tsui, "Development of a computer-generated model for the coronary arterial tree based on multislice CT and morphometric data," *Medical Imaging 2006: Physics of Medical Imaging* **6142**, (2006).

Methodology for generating a 3D computerized breast phantom from empirical data

Christina M. Li^{a)}

Department of Radiology and Biomedical Engineering, Carl E. Ravin Advanced Imaging Laboratories, Duke University Medical Center, Durham, North Carolina 27705

W. Paul Segars

Department of Radiology and Biomedical Engineering and Medical Physics Graduate Program, Carl E. Ravin Advanced Imaging Laboratories, Duke University Medical Center, Durham, North Carolina 27705

Georgia D. Tourassi

Department of Radiology and Medical Physics Graduate Program, Carl E. Ravin Advanced Imaging Laboratories, Duke University Medical Center, Durham, North Carolina 27705

John M. Boone

Department of Radiology, X-ray Imaging Laboratory, Davis Medical Center, University of California, Sacramento, California 95817

James T. Dobbins III

Department of Radiology and Biomedical Engineering and Medical Physics Graduate Program, Carl E. Ravin Advanced Imaging Laboratories, Duke University Medical Center, Durham, North Carolina 27705

(Received 13 February 2009; revised 25 April 2009; accepted for publication 30 April 2009; published 12 June 2009)

The initial process for creating a flexible three-dimensional computer-generated breast phantom based on empirical data is described. Dedicated breast computed-tomography data were processed to suppress noise and scatter artifacts in the reconstructed image set. An automated algorithm was developed to classify the breast into its primary components. A preliminary phantom defined using subdivision surfaces was generated from the segmented data. To demonstrate potential applications of the phantom, simulated mammographic image data were acquired of the phantom using a simplistic compression model and an analytic projection algorithm directly on the surface model. The simulated image was generated using a model for a polyenergetic cone-beam projection of the compressed phantom. The methods used to create the breast phantom generate resulting images that have a high level of tissue structure detail available and appear similar to actual mammograms. Fractal dimension measurements of simulated images of the phantom are comparatively similar to measurements from images of real human subjects. A realistic and geometrically defined breast phantom that can accurately simulate imaging data may have many applications in breast imaging research. © 2009 American Association of Physicists in Medicine. [DOI: [10.1118/1.3140588](https://doi.org/10.1118/1.3140588)]

Key words: breast imaging, mammography, phantom, segmentation, modeling

I. INTRODUCTION

Early detection of breast cancer has been instrumental in reducing the mortality of the disease.¹ Many new and improved imaging systems and techniques are currently under development for the detection and diagnosis of breast cancer. It is essential for the advancement of breast imaging systems to have a tool that can be used to optimize and evaluate new techniques and to compare methods across different modalities.

Phantoms are often employed to optimize imaging parameters and improve image quality by providing a “known truth” to evaluate new reconstruction algorithms and aid in the development of novel imaging techniques. Physical phantoms used in breast imaging are currently limited in that they cannot adequately represent the variety of breast sizes, shapes, compositions, and parenchymal detail. It would be difficult to generate patient-specific physical phantoms due

to the time consuming production process and the expense of the materials that compose the phantoms. Computerized phantoms, on the other hand, are advantageous in that they can be modified in terms of size and tissue distribution to generate any number of anatomical variations present in a patient population. The anatomy and physiology are user defined so they provide a known truth from which to evaluate imaging devices and techniques without additional material costs and production time other than software processing.

There have been several computerized three-dimensional (3D) breast phantoms created; all were based either on voxelization of real subject data or mathematical models based on geometric primitives.^{2–10} These computerized breast imaging phantoms have used different approaches, each with its own limitations. Mathematical breast phantoms are flexible and can model varying compositions of breasts, but they are too simplistic in their representation of breast tissue, and the resultant images are qualitatively unrealistic. Voxelized

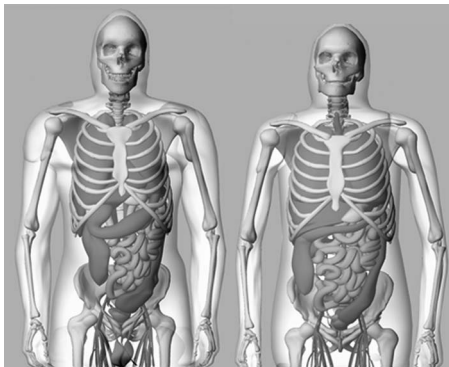


FIG. 1. Surface renderings of the 4D XCAT male (left) and female (right) anatomy.

breast phantoms offer a more realistic approach since they are based on actual imaging data; however, they are modeled after a single breast and do not offer the flexibility needed to represent the variability present in the patient population. In addition, several of the recently introduced voxelized phantoms are based on high-dose breast computed tomography (CT) of mastectomy specimens. These specimens do not adequately represent intact breasts, since they were placed in holders and contain air pockets. There is clearly a need for a realistic and flexible computerized breast phantom.

There are many potential applications in breast imaging research for a phantom with these attributes. Many emerging modalities such as tomosynthesis, dual-energy mammography, elastography, CT, ultrasound, and dynamic contrast-enhanced breast MRI would benefit from having an accurate and validated model of the breast to allow imaging procedures to be optimized under clinically relevant conditions. The effects of acquisition parameters (e.g., number and angular spacing of projections in tomosynthesis), physical processes (e.g., scatter, beam hardening, and heel effect), and sources of variability (e.g., patient anatomy, dose, and positioning) can all be evaluated and studied in tandem or independently using patient-quality simulated data. A realistic computerized phantom would also provide the necessary framework with which to quantitatively compare the effectiveness of different imaging methods in tasks that model clinical practice such as lesion detection. Collaborating or multidisciplinary groups can share the same virtual phantom without having to transport a physical phantom around and impartial comparison can be performed using the same phantom to evaluate claims from competing groups for publication or regulatory approval.

Recent work in phantom development has focused on the creation of more realistic, mathematically based models using techniques from computer graphics. One such phantom is the four-dimensional (4D) extended cardiac-torso (XCAT) phantom (Fig. 1)¹¹ that was developed by Segars *et al.* to provide a realistic, flexible, anatomical, and physiological model of the human body for use in imaging research.^{12–14} Based on patient data and using nonuniform rational b-spline (NURBS) surfaces to define the anatomy, the XCAT phantom combines a voxelized approach with a mathematical one

to offer a phantom with realistic and detailed organs that remain flexible to allow for anatomical variation and organ deformation. The XCAT phantom includes detailed whole body models for the male and female anatomy based on the visible human data from the National Library of Medicine.

When combined with accurate models of the imaging process (e.g., SPECT, PET, MRI, ultrasound, and CT) the 4D XCAT is capable of simulating realistic imaging data close to those of actual patients. The XCAT phantom has gained widespread use in medical imaging research for evaluating and improving instrumentation, data acquisition, and image processing and reconstruction methods.

Despite this success, the XCAT is limited in its applications to breast imaging research. The female anatomy of the XCAT phantom only uses a simple outer surface to model the breast and does not include any detailed structures. In addition, the phantom was created using data from a single patient and does not simulate breast variations among different women.

The goal of the work described in this paper was to create a detailed 3D computer-generated breast phantom based on empirical data obtained from breast CT of human subjects. The breast phantom will be incorporated into the 4D XCAT phantom in order to make it applicable to breast imaging research. To the best of our knowledge, this will be the first breast phantom based on real human data with the ability to simulate a variety of sizes, compositions, and deformations. The work presented here describes the methods we used to create an initial phantom based on high-resolution breast CT data of a single human subject and demonstrates the phantom's ability to simulate multimodality imaging data.

II. METHODS

II.A. Overview

Developing a realistic and useful breast phantom requires many different steps: One must (1) acquire volumetric imaging data, (2) classify the different components of breast tissue as adipose, fibroglandular, or skin, (3) create a flexible model of the breast from the segmented data, and (4) develop realistic methods to simulate compression. Once the phantom is developed, it may be compressed or left uncompressed depending on the modality (x-ray, MR, ultrasound, SPECT, PET) and computer-based simulation methods can be applied to it to generate realistic imaging data.

Any imaging data may be used as the basis for the phantom. For our particular application, we chose dedicated breast CT data due to their high-resolution detail. Depending on the data selected for the phantom, different image processing techniques need to be applied to it so as to facilitate segmentation of the data. Once a data set is segmented, flexible surface models can be created for each breast tissue. We define each structure in the breast using subdivision surfaces.¹⁵ Unlike the NURBS surfaces that define the XCAT phantom, subdivision surfaces have the ability to model complicated branching structures (e.g., the fibroglandular tissue) with a single surface. NURBS surfaces would require defining a surface for each branch, meaning the structure

would be composed of many tiny NURBS surfaces. Subdivision surfaces are, therefore, much better for modeling the complicated structures of the breast. A detailed description of the steps used experimentally to create our phantom is given below.

II.B. Breast CT data acquisition and image processing

As mentioned above, the breast phantom designed in this work is based on CT data which provide a high-resolution detailed anatomy in its natural form. Dedicated breast CT is currently an investigational tool that may eventually have applications in breast cancer screening or diagnostic evaluation. Dedicated breast CT system images reduce anatomical noise from overlapping structures and provide a clear depiction of 3D anatomical detail that will be useful for phantom creation.

There are several groups currently researching dedicated breast CT at the University of California at Davis,^{16–22} Duke University,^{23–31} University of Rochester,^{32–36} University of Massachusetts Medical School,^{37–39} and University of Texas M.D. Anderson Cancer Center.^{40,41} CT image data used in this study were obtained from investigators at the University of California at Davis as part of an IRB approved study using a prototype dedicated breast CT scanner.

The patient lies in the prone position on a scanning table with the pendant breast hanging through an opening in the table without compression. The gantry rotates over 360° in the horizontal plane around the breast and acquires 500 cone-beam projection images in 16.6 s. Each breast is scanned separately and the mean fibroglandular radiation dose delivered to the breast was constrained to be the same as two-view mammography.^{16–22}

The low-dose acquisition of the breast data as well as the cone-beam geometry of the CT system results in image degradation due to scatter radiation and considerable quantum noise. Therefore correction of scatter and noise is a necessary part of this project because the nonuniformity of the background may cause the denser tissue (fibroglandular tissue) values to be lower than the less-dense (adipose tissue) values and vice versa. This presents a problem when the segmentation of breast CT data is performed using value-based techniques in order to create the breast model. Algorithms were implemented to reduce noise and correct for scatter in the breast CT images as described below.

II.B.1. Noise reduction

A denoising algorithm developed by Xia *et al.*^{42,43} was used in order to suppress noise in breast CT projection images prior to reconstruction without loss of spatial resolution. In a breast CT projection image, the noise is larger toward the chest wall, and when the dose is reduced, this phenomenon becomes more pronounced. The method of Xia *et al.* removes noise with a spatially adaptive partial diffusion equation technique that takes into account the nonuniform distribution of noise in the projection images. The projection images were processed with 40 iterations of the denoising

algorithm of Xia *et al.* instead of the recommended 10 iterations based on subjective evaluation of the effect of noise suppression on subsequent segmentation. Tomographic images were reconstructed using a custom written Feldkamp filtered backprojection algorithm^{42,43} and generated 255 768×768 images with an in-plane resolution of 250 μm and slice thickness of 500 μm. The slice thickness was chosen based on having sufficient data for phantom creation. To demonstrate the noise reduction achieved with the denoising algorithm, the projections were processed using different numbers of denoising iterations (0,10,40) before reconstruction. Ten 100×100 regions of interest (ROIs) were chosen across ten slices throughout the reconstructed image volumes and the mean of the standard deviations of these ROIs was measured.

II.B.2. Scatter correction

A postreconstruction scatter correction technique was implemented to correct for background nonuniformity in each axial image.⁴⁴ The cupping artifact due to scatter radiation is modeled as a circularly symmetric additive background signal profile in the reconstructed breast images. The artifact lowers the true tissue signal in a nonuniform way with a greater bias toward the breast center. The correction signal is based on a sampling technique to obtain an estimate of the adipose tissue signal in the axial images. The center of each axial slice was defined and the minimum value of each radius was used to generate an estimate of the adipose tissue signal. Any inconsistencies or trends across the adipose tissue signal were assumed to be from scatter and were manifested in the axial image as a cupping artifact. A second degree polynomial was fitted to each axial slice estimate for the adipose tissue signal. The values for the polynomial function were averaged across all slices and used to simulate the cupping artifact in each slice. The second degree polynomial used for correction was $0.13x^2 - 0.64x + 9858$. The simulated cupping artifact was subtracted from the breast volume in order to correct for scatter.

II.C. Tissue segmentation

After noise and scatter correction, the next step is the automated classification of the CT data into the various breast tissues that will define the appropriate physical characteristics of each pixel during simulated compression and image acquisition. Pixels were categorized as adipose, fibroglandular, or skin.

II.C.1. Breast masking

The first step in segmentation is to define a binary mask for both the breast volume and the skin. The breast mask is used to target the segmentation to the breast volume and not the background. This mask also serves to classify the adipose tissue by default, since the algorithm will assume that everything within the breast volume that is not classified as fibroglandular tissue or skin will be classified as adipose tissue. Several steps are used to define the mask including thresh-

olding, filtering, and morphological operations. The breast volume mask can be defined with a threshold between the background and breast tissue. However, the threshold needs to be tuned to each breast volume since the noise reduction and scatter correction image processing steps may change the values of the data.

The order of binary masking performed is not critical to the overall performance of the phantom. In the experimental method described, the skin mask was defined first since the skin mask requires a nonmasked image to create and masking of the entire breast volume is done directly after the breast mask definition.

II.C.1.a. Breast skin mask definition. To define a mask for the skin, the local standard deviation of each axial slice was determined using the MATLAB `stdfilt` function. The `stdfilt` function requires a structuring element, which was defined as a ball of height and radius of six pixels. The output of `stdfilt` was normalized and thresholded using 0.1 as the cutoff. To define a mask for the skin, the result was morphologically dilated to ensure full skin coverage with the skin mask. The dilation structuring element used was a disk of radius of six pixels. The values used were determined by trial and error for a single example breast.

II.C.1.b. Breast mask definition. The breast volume mask can be defined with a threshold between the background and breast tissue. However, the threshold needs to be tuned to each breast volume since the different image processing steps may change the values of the data. To define a mask for the breast volume, all pixels that were less than 8000 in value were set equal to zero. The remaining breast was morphologically opened using a disk structuring element with a radius of 20 pixels. This ensured that all pixels within the breast volume would be maintained even if some were below 8000 in value. A threshold was found using the MATLAB `graythresh` function and the mask for the breast was defined with this value. The mask was applied to the breast such that all values not defined with the mask were set to zero.

II.C.2. Iterative histogram classification

After the mask was applied to the breast data, all that remained was the breast tissue. A histogram classifier was used to differentiate between adipose and other types of tissues due to differences in their pixel values. Based on a method developed by Packard and Boone,⁴⁵ an initial segmentation of the breast tissues is done by iteratively evaluating the histograms of each axial slice. The histogram for each axial slice of the scatter corrected breast was found. The left and right edges were used to define the center of the histogram. The mean of the left and right sides of the histogram were found and used as the left and right bounds to redefine the center. This process was repeated until there was little to no change in the center value between iterations. The signal containing the center values of each slice was smoothed with a seven-point moving average filter. A second degree polynomial was fitted to the data and the first 60 values were replaced with the moving average filter output. This maintained the larger values near the chest wall and

minimized large swings in the signal. The smoothed signal was used to define the threshold point for each slice such that all values above the smoothed center value were classified as fibroglandular and skin, and all values below were considered to be adipose tissue and are classified as zero. This process left each axial slice of the segmented volume containing an initial segmentation of only fibroglandular and skin tissues.

II.C.3. Breast skin definition and removal

After the initial histogram segmentation, the skin mask was applied. The histogram classifier does not differentiate between skin and fibroglandular tissues; therefore the predefined mask was used for skin definition. All nonadipose tissue specified by the histogram classifier that lies within the skin mask was classified as skin. The segmented skin was saved and removed from the segmented breast and all following steps were performed only on the remaining classified fibroglandular tissue. In addition, single pixel islands that were likely to be residual mis-segmented adipose tissue were removed. All remaining steps were performed on fibroglandular tissue only.

II.C.4. Predefined morphological functions

A binary volume of the fibroglandular tissue was created, and in each axial slice the MATLAB `bwareaopen` function was used to remove any groups of pixels in the slice that contained fewer than five pixels. Then a series of MATLAB `bw-morph` operations was performed to fill in, or bridge, missing pixel connections.

II.C.5. Ellipsoidal connection algorithm

There remained several small groups of less than 50 pixels that visually appeared to be disconnected from nearby groups of pixels. The size was chosen based on the current data set after visually inspecting islands that were known to be connected based on the CT data and disregarding islands that were too large. However, some islands were disjointed sections that appeared as linear objects and appeared to be connected to islands in the current slice and some were circular and appeared to continue through to the next slice. Therefore, it was necessary to differentiate between circular islands and linear islands. In order to define and link the appropriate sections together, the ellipsoidal shape of the islands was evaluated using the MATLAB `regionprops-eccentricity` function. The island was classified as closer to a line and possibly connected in the current plane if it had greater than 85% eccentricity and close to a circle and connected to the next plane if it was less. This differentiation was made assuming that any fibers going between planes would appear rounder than fibers staying within the plane. If an island was found to have greater than 85% eccentricity and an area of less than 50 pixels, then it was considered a candidate for linking to another nearby island. If another group of pixels was within 20 pixels away and along the angular orientation of the candidate island, then the line connecting them was labeled as fibroglandular tissue. This was

done by using MATLAB `imclose` function with a line structuring element of length of 20 pixels at the designated angular orientation.

II.C.6. Targeted region growing

After the previous step identified probable islands (small and linear ellipses) that were supposed to be joined, there were still certain areas that should be joined and were not identified as small linear ellipses. The targeted region-growing algorithm was used to join these regions. It defines the distance between islands and searches for short ladder patterns and then classifies the ladder as part of the fibroglandular tissue. This step joined together separated islands that were located close enough to indicate that they should be connected. In order to address missing connections for regions that were larger than 50 pixels and not linear in shape, it was necessary to extend these regions under specific conditions such that the original shape and size of each region were essentially preserved by growing only under certain conditions. It was assumed that regions that should be joined would be relatively close together and there would be a specific short path between them. To find distances between regions, the MATLAB `bwdist` function was used to define a distance map for each binary axial slice of classified fibroglandular tissue. Ladderlike patterns in the distance map were searched for at 10° angular increments from -85° to 85° , such as

$$\begin{bmatrix} 1 & 2 & 3 & 2 & 1 \end{bmatrix}, \quad \begin{bmatrix} 1 \\ 2 \\ 3 \\ 2 \\ 1 \end{bmatrix}, \quad \text{and} \quad \begin{bmatrix} 1 & 0 & 0 & 0 & 0 \\ 0 & 2 & 0 & 0 & 0 \\ 0 & 0 & 3 & 0 & 0 \\ 0 & 0 & 0 & 2 & 0 \\ 0 & 0 & 0 & 0 & 1 \end{bmatrix}.$$

If the pattern was found, it was classified as fibroglandular tissue. The maximum ladder distance was five pixels for the axial slices.

II.C.7. Volumetric processing

Up to this point, all of the segmentation has been performed only in axial planes. There may remain some discontinuities between slices due to the two-dimensional (2D) processing. In order to join the fibroglandular tissue volumetrically and smooth away the discontinuities between the axial slices, the MATLAB predefined morphological functions, ellipsoidal connection algorithm, and targeted region growing were performed on the coronal and sagittal slices. The MATLAB `bwmorph` function was used on the classified axial slices to fill in any small holes prior to processing in the coronal and sagittal directions. The values used for the different functions during volumetric processing were that the candidate region area for the ellipsoidal connection algorithm was 30 with eccentricity of 0.85, and the maximum ladder distance used for the targeted region-growing algorithm was 3.

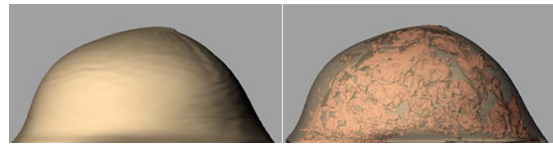


FIG. 2. Surface rendering of the skin is shown on the left and an illustration of the inner structures is on the right.

II.C.8. Density differentiation

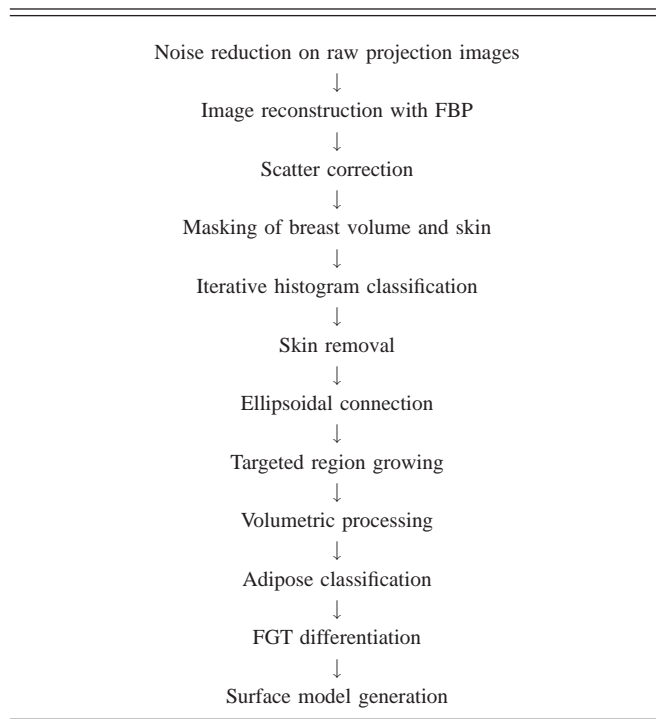
Although the breast is composed primarily of the three segmented tissue types, there is often a compositional marbling effect, where fibroglandular and adipose tissues are interspersed in varying degrees. This marbling effect is visible in the reconstructed data where some fibroglandular regions appear less dense and have a pixel value between that of adipose and fibroglandular tissues. The segmentation algorithm takes into account the varying levels of adipose content in the fibroglandular tissue by dividing the segmented fibroglandular tissue into three regions based on pixel value. The algorithm results in the breast segmented into five components: adipose, skin, and three varying levels of fibroglandular tissue.

After the volumetric processing step, the fibroglandular tissue had been classified as well as the skin. All pixels located within the predefined mask for the breast that were not skin or fibroglandular tissue pixels were classified as adipose tissue. The histogram of the fibroglandular tissue breast pixels was determined and divided into four segments. Because the fibroglandular tissue density visually appeared to consist primarily of less-dense tissue, the density differentiation was skewed toward the lower half. The first two segments were further classified as primarily adipose tissue with a low percentage (25%) of fibroglandular tissue. The third segment was classified as 75% fibroglandular tissue and the fourth segment was classified as 100% fibroglandular tissue. This differentiation incorporated the marbling property of the different breast tissues. Three fibroglandular levels were chosen because this provided a balance between simplicity and realism for the resulting segmented data; fewer levels would not provide a model with enough realism and higher levels were unnecessary because it complicated the final model and did not increase the realism of the final image.

II.D. Breast surface mesh-model creation

After the breast was segmented a polygon mesh model of each classified tissue was created using the MATLAB `isosurface` function, which renders isosurfaces in volumetric data. The `isosurface` function was used to generate initial polygon mesh objects for the skin, fibroglandular, and adipose tissues. Figure 2 shows an example surface rendering from this mesh model of the segmented breast CT data. The polygon mesh created for each structure using MATLAB serves as the initial mesh of a subdivision surface. The mesh can be iteratively subdivided and smoothed to create a smooth surface. Table I summarizes the methods we used to create the breast phantom.

TABLE I. Methodology to create breast phantom.



II.E. Simulated compression

To be applicable to many breast imaging modalities, the breast phantom created above must be able to simulate different compression levels. Currently, we use a simple model to simulate compression. The details of this algorithm have been presented in detail previously, but in general, the breast is compressed in one dimension (x) and extended in the other dimensions (y and z) simulating compression between stiff plates.⁴⁶ The breast is assumed to be incompressible (fixed volume) and isotropic. The mesh's node locations were determined to be inside or outside the compressed thickness of the breast. Each x value of the vertices located outside is multiplied by the compression ratio to give the new x values for the compressed vertex location. Each x value of the vertices originally located between the simulated compression paddles remained unchanged. The method is demonstrated in Fig. 3.

II.F. Simulated radiographic images

Once the phantom is defined, it can be combined with existing simulation packages to simulate imaging data. To demonstrate the application of the phantom, we simulate



FIG. 3. Illustration of breast compression geometry.

mammography and tomosynthesis data from the phantom as described below. Both of these modalities require compression of the breast.

The vertices of the mesh-model were input into our simplified compression algorithm in order to simulate the geometry of the breast for simulated mammographic imaging. The breast was compressed down to a thickness of 5 cm.

X-ray projection images were simulated directly from the surface mesh model using a technique developed by Segars *et al.*¹¹ The geometry of the system was equivalent to that of the Siemens Mammomat Novation System presented previously by the authors.⁴⁶ Attenuation coefficients for adipose, fibroglandular, and skin were derived from International Commission on Radiation Units and Measurements (ICRU) tissue data.⁴⁷ The three different levels of fibroglandular tissue were assigned attenuation coefficients between adipose and muscle in order to account for their relative amount of marbling. The most dense fibroglandular tissue was assigned the elemental composition of muscle for our purposes since fibroglandular tissue was not available in the database used. A custom polyenergetic spectrum was used to simulate a 50 μm rhodium filter with a tungsten target.⁴⁸ Images were simulated with 1000×1000 pixels at 250 μm resolution.

After a simulated projection was acquired, a sigmoidal correction function was applied in order to simulate a screen-film mammogram, similar to what is currently applied to digitally acquired mammograms. To validate the mammogram simulation, the fractal dimension (FD) was calculated for ROIs from the simulated mammogram and compared to typical FD values obtained from real mammograms.^{49–51} Ten different 150×150 ROIs located near the nipple were used for the FD measurement. The FD was estimated using the circular average power spectrum method^{52,53} that has been used successfully in prior mammography applications.⁵⁴ Initially, the two-dimensional power spectrum of the image was obtained using zero padding and a radial Hamming window to ensure better estimation of the power spectrum.^{55,56} The 2D power spectrum was then transformed into one dimension by linear averaging the spectrum as a function of the radial distance from zero frequency. The Fourier power spectrum was plotted on a log-log scale as a function of the frequency and linear regression was applied to estimate the slope of the fitted line. The slope was then transformed into a FD measure as described by Tourassi *et al.*⁵⁴

III. RESULTS

III.A. Image processing

Figure 4 illustrates the denoising algorithm's effect on the original images. It clearly removes a significant amount of noise and provides for clearer visualization of the fibroglandular tissue in the denoised data. Table II shows that the average standard deviation of ten 100×100 ROIs decreases as the number of denoising iterations increases, which demonstrates the noise reduction due to denoising. Figure 5 illustrates the signal that was subtracted from each slice in order to perform postreconstruction scatter correction to remove the cupping artifact.

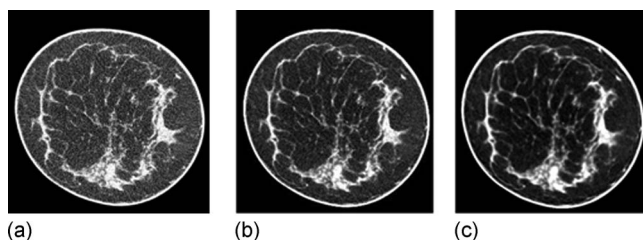


FIG. 4. (A) The original reconstructed CT data. (B) The data with ten denoising iterations, as optimal for image review. (C) The data with 40 denoising iterations to perform maximum noise reduction for segmentation purposes only.

III.B. Tissue segmentation

Figure 6 shows the signal that contains the threshold during iterative histogram classification for each axial slice. Both the originally determined threshold level and the applied smoothed level values are shown.

Figure 7 is the binary data used during segmentation and illustrates the effect of using predefined morphological operations along with the ellipsoidal connection algorithm and targeted region growing to classify the fibroglandular data. Although subtle, there is improvement with the ellipsoidal connection algorithm and targeted region growing. These methods add noticeably to the high-resolution detail of resulting images simulated with the phantom without perturbing the overall shape and structure of the breast tissue.

Figure 8 illustrates the output of classification from the volumetric processing step of the described algorithm. Performing the segmentation steps volumetrically fills in holes between neighboring slices and further improves the classification performance.

Figure 9 shows the final segmented slice. The density differentiation is shown, which more closely represents the real data than using a single value to describe the fibroglandular tissue.

III.C. Simulated radiographic images

Figure 10 shows the characteristic curve that was used on simulated projection images in order to simulate screen-film mammogram appearance. Figure 11 shows a comparison of a mammogram of a real human subject with two simulated mammograms of the breast phantom. Figure 11(A) shows an actual mammogram of a real human subject that is different than the subject used for the phantom generation. Figure 11(B) shows a mammogram of the phantom using defined attenuation coefficients ranging from adipose to muscle for the differentiated fibroglandular tissue. Figure 11(C) shows a

TABLE II. Comparison of standard deviations for different levels of denoising.

Original data	Denoised data	Denoised data
(0 iterations)	(10 iterations)	(40 iterations)
0.119 ± 0.013	0.07 ± 0.011	0.057 ± 0.011

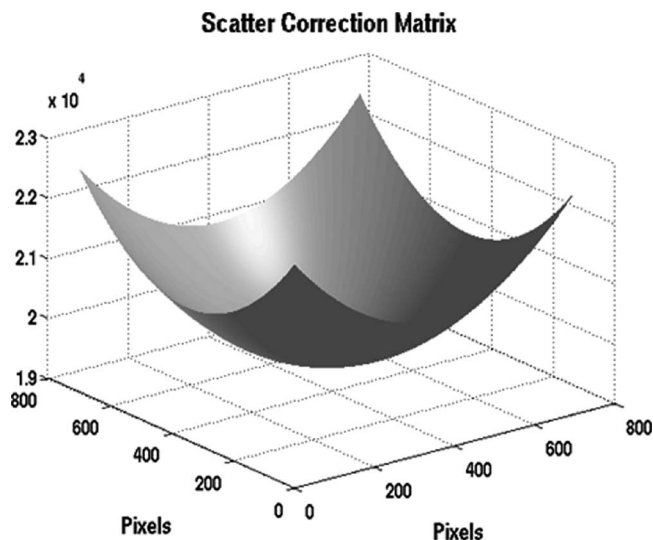


FIG. 5. Signal matrix subtracted from each slice to correct for the cupping artifact due to scatter.

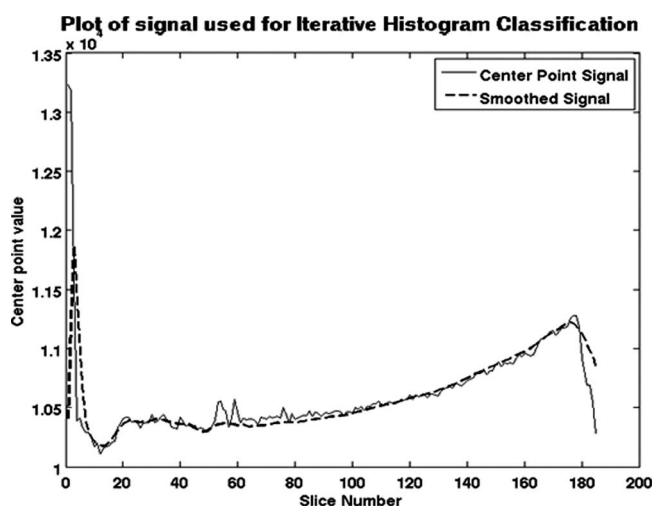


FIG. 6. Signal of threshold points used for iterative histogram classification.

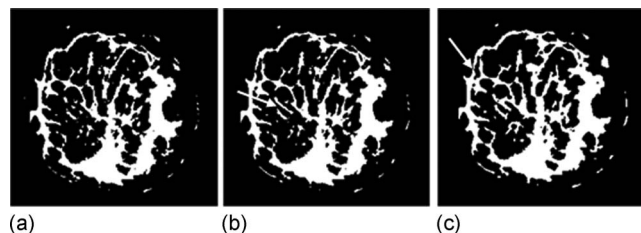


FIG. 7. (A) The initial binary slice after histogram classification. (B) The slice after the ellipsoidal connection algorithm. (C) The slice after targeted region growing. Arrows show regions added with the algorithm.

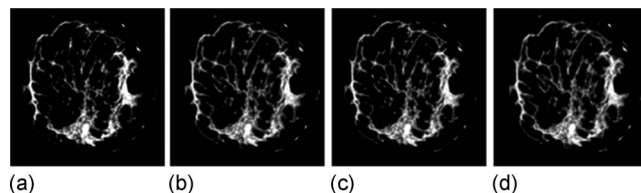


FIG. 8. (A) Result from iterative histogram classification. (B) Result from axial processing. (C) Result from sagittal processing. (D) Result from coronal processing.

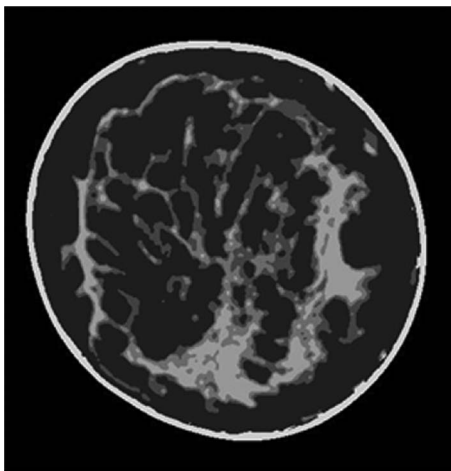


FIG. 9. Final segmented slice showing five different tissue density classifications. From darkest to lightest: adipose, fibroglandular 1, fibroglandular 2, fibroglandular 3, skin.

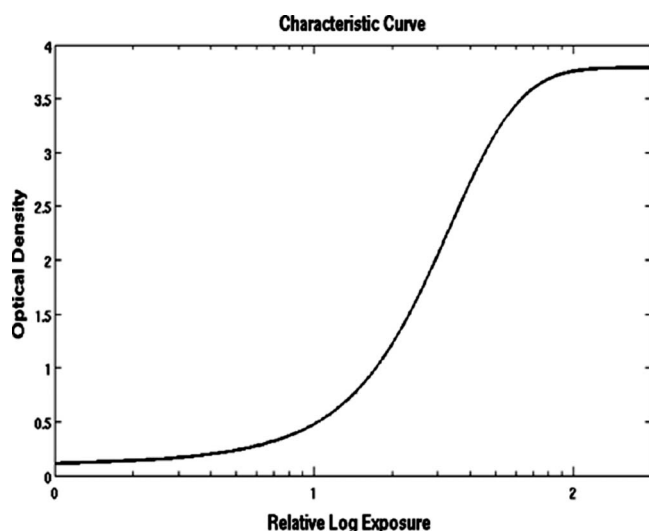


FIG. 10. Characteristic curve used on simulated projection image in order to simulate mammogram.

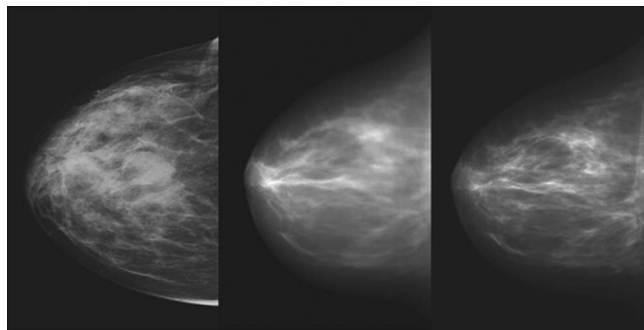


FIG. 11. (A) An example of a real mammogram for comparison purposes of a different subject than used to generate the computerized breast phantom. (B) The mammogram with defined attenuation coefficients that are described with three levels of fibroglandular tissue ranging from adipose to muscle. (C) The mammogram with enhanced attenuation coefficient to demonstrate high-resolution detail of the phantom.

TABLE III. Comparison of the FD distributions calculated from simulations to published results observed from actual mammograms.

Fractal dimension (the mean and standard deviation are displayed)	Hamming window	Published results (Ref. 49)
Simulated mammogram [Fig. 11(B)]	2.23 ± 0.007	2.36 ± 0.10
Simulated mammogram [Fig. 11(C)]	2.18 ± 0.016	

mammogram of the phantom with artificially enhanced attenuation coefficients to illustrate the high resolution detail. The simulated mammograms subjectively demonstrate the realism of the phantom and the level of detail in the tissue structures appears similar to actual mammograms.

A quantitative validation of the breast phantom simulations was performed using the fractal dimension calculated from ROIs of the simulated mammograms [Figs. 11(B) and 11(C)]. The average results from the simulation are shown in Table III as compared to a study from Bakic *et al.* performed on actual mammograms.⁴⁹ The simulated results compare quantitatively to published findings. They also compare similarly to other studies by Caldwell *et al.*⁵⁰ and Byng *et al.*⁵¹ that have found the FD to be within the range of 2.25–2.6.

IV. DISCUSSION

The goal of producing a suitable breast phantom for research has been pursued by a number of investigators and presents many challenges. Physical phantoms are not adjustable and do not realistically mimic the complexity of breast anatomy. Computerized phantoms, on the other hand, have traditionally offered either improved realism or flexibility but often not at the same time. Computerized phantoms have been available in two types: voxelized phantoms and mathematical phantoms based on geometric primitives. Voxelized phantoms are based on real human data and are realistic; however, they are not flexible and are also limited by the parameters and environment used to acquire the images: such phantoms may include arbitrarily fashioned mastectomy specimens or low-resolution full body CT data. Mathematical phantoms allow for flexibility; however, the simplistic shapes used as their basis do not generate visually realistic images. The breast phantom created with this method differs from other breast phantoms in that it combines the realism of a voxelized phantom with the flexibility of a mathematical phantom.

Initial images generated using this new methodology demonstrate the realistic high-resolution detail available with this phantom. However, several areas remain that require further investigation. There are artifacts around the nipple region that may likely be due to the mesh creation or the image acquisition algorithm. Further optimization may be required for the final phantom to reduce the number of triangles in order to simplify and smooth the surface model. The goal of mesh optimization is to decrease the complexity while minimally perturbing the overall shape and improving the fit to the data. This optimized mesh will then become the input to

the subdivision surface algorithm that will generate the final mesh to be incorporated into the XCAT phantom.

Certain high-resolution detail structures such as Cooper's ligaments are not fully visible because the segmentation was not able to robustly classify these structures. Mathematically defined fine resolution structures can be incorporated in the future to artificially enhance the detail visible in the final acquired image without significantly affecting the phantom's realism.

Although fast and efficient, the image simulation method will be further improved to include models for noise, detector effects, and beam hardening. These steps will result in more realistic noise levels and statistics. The current model used a simplistic compression algorithm. This does not take into consideration the different mechanical properties of the different tissues. In the future, finite element methods will be implemented to realistically simulate the deformation of breast tissue under compression.

The similarity between the FD calculated from the simulated mammograms compared to the FD of real mammograms reported in the literature demonstrate the realism of the breast phantom and that the simulation methods used are capable of producing realistic imaging data. In addition, the phantom has visually demonstrated that there is a realistic level of detail that requires some additional tuning to further improve its utility.

The described phantom includes information from only a single patient. In the future, many additional models will be created from different human subject data and the final phantoms methodology will incorporate information from all of the models. We plan to incorporate adjustable size, density, and tissue distribution in order to simulate a large number of simulated subjects. Information from the multiple segmented data sets will be synthesized to create a generic base breast template that can be incorporated into the XCAT phantom. The base breast template can be manipulated to model a breast of any size or composition and deformed to simulate compression, essentially creating a source for an infinite number of simulated breasts to investigate existing and emerging breast imaging modalities.

V. CONCLUSION

Current breast phantoms have many limitations. The phantom presented in this work combines the flexibility of a mathematical phantom with realistic anatomy based on actual human data. This new phantom may provide an important tool for breast imaging researchers to optimize and improve different imaging techniques and to evaluate and compare various breast imaging modalities in terms of clinical performance.

ACKNOWLEDGMENTS

Grant support for this project was provided by the Department of Defense Breast Cancer Research Program (Grant No. W81XWH-06-1-073), National Institutes of Health (NIH) (Grant No. R01EB001838), NIH/NCI (Grant No. R01CA112437), and NIH/NCI (Grant No. R01CA94236).

The authors would like to acknowledge the help and support provided by Dr. Jessie Q. Xia for the use of the denoising algorithm, Dr. Joseph Y. Lo and Seimens Healthcare for providing the sample mammogram of the real human subject, and Dr. Jay A. Baker for reviewing simulated images of the phantom and providing valuable feedback.

^a)Electronic mail: christina.li@duke.edu

¹ACS, *American Cancer Society: Cancer Facts and Figures 2008* (American Cancer Society, Atlanta, GA, 2008).

²T. Han et al., "Simulation of mammograms and tomosynthesis imaging with cone beam breast CT images," *Proc. SPIE* **6913**, 17.1–17.7 (2008).

³P. Bakic, M. Albert, D. Brzakovic, and A. Maidment, "Mammogram synthesis using a 3D simulation. I. Breast tissue model and image acquisition simulation," *Med. Phys.* **29**, 2131–2139 (2002).

⁴P. Bakic, M. Albert, D. Brzakovic, and A. Maidment, "Mammogram synthesis using a 3D simulation. II. Evaluation of synthetic mammogram texture," *Med. Phys.* **29**, 2140–2151 (2002).

⁵P. Bakic, M. Albert, D. Brzakovic, and A. Maidment, "Mammogram synthesis using a three-dimensional simulation. III. Modeling and evaluation of the breast ductal network," *Med. Phys.* **30**, 1914–1925 (2003).

⁶K. Bliznakova, Z. Bliznakov, V. Bravou, Z. Kolitsi, and N. Pallikarakis, "A three-dimensional breast software phantom for mammography simulation," *Phys. Med. Biol.* **48**, 3699–3719 (2003).

⁷J. Shorey, "Stochastic simulations for the detection of objects in three dimensional volumes: Applications in medical imaging and ocean acoustics," Ph.D. thesis, Duke University, 2007.

⁸C. Hoeschen et al., "A high-resolution voxel phantom of the breast for dose calculations in mammography," *Radiat. Prot. Dosimetry* **114**, 406–409 (2005).

⁹L. Zhou, J. Oldan, P. Fisher, and G. Gindi, "Low-contrast lesion detection in tomosynthetic breast imaging using a realistic breast phantom," *Proc. SPIE* **6142**, 5A.1–5A.12 (2006).

¹⁰J. M. O'Connor, M. Das, C. Didier, M. Mah'D, and S. J. Glick, "Using mastectomy specimens to develop breast models for breast tomosynthesis and CT breast imaging," *Proc. SPIE* **6913**, 15.1–15.6 (2008).

¹¹W. P. Segars, M. Mahesh, T. J. Beck, E. C. Frey, and B. M. W. Tsui, "Realistic CT simulation using the 4D XCAT phantom," *Med. Phys.* **35**, 3800–3808 (2008).

¹²W. P. Segars, "Development and application of the new dynamic NURBS-based cardiac-torso (NCAT) phantom," Ph.D. thesis, University of North Carolina, 2001.

¹³W. P. Segars, M. Mahesh, T. Beck, E. C. Frey, and B. M. W. Tsui, "Validation of the 4D NCAT simulation tools for use in high-resolution x-ray CT research," *Proc. SPIE* **5745**, 828–834 (2005).

¹⁴W. P. Segars, B. M. W. Tsui, E. C. Frey, and E. K. Fishman, "Extension of the 4D NCAT phantom to dynamic x-ray CT simulation," *IEEE Nuclear Science Symposium Conference* **5**, 3195–3199 (2003).

¹⁵H. Hoppe et al., "Piecewise smooth surface reconstruction," *Computer Graphics Proceedings, Annual Conference* **28**, 295–302 (1994).

¹⁶K. Yang, A. L. Kwan, and J. M. Boone, "Computer modeling of the spatial resolution properties of a dedicated breast CT system," *Med. Phys.* **34**, 2059–2069 (2007).

¹⁷J. M. Boone et al., "Performance assessment of a pendant-geometry CT scanner for breast cancer detection," *Proc. SPIE* **5745**, 319–323 (2005).

¹⁸J. M. Boone, T. R. Nelson, K. K. Lindfors, and J. A. Seibert, "Dedicated breast CT: Radiation dose and image quality evaluation," *Radiology* **221**, 657–667 (2001).

¹⁹K. K. Lindfors et al., "Dedicated breast CT: Initial clinical experience," *Radiology* **246**, 725–733 (2008).

²⁰J. M. Boone et al., "Computed tomography for imaging the breast," *Journal of Mammary Gland Biology and Neoplasia* **11**, 103–111 (2006).

²¹A. L. C. Kwan, J. M. Boone, and N. Shah, "Evaluation of x-ray scatter properties in a dedicated cone-beam breast CT scanner," *Med. Phys.* **32**, 2967–2975 (2005).

²²A. L. C. Kwan, J. M. Boone, K. Yang, and S. Huang, "Evaluation of the spatial resolution characteristics of a cone-beam breast CT scanner," *Med. Phys.* **34**, 275–281 (2007).

²³M. P. Tornai et al., "Design and development of a fully-3D dedicated x-ray computed mamotomography system," *Proc. SPIE* **5745**, 189–197 (2005).

- ²⁴R. L. McKinley, C. N. Brzymialkiewicz, P. Madhav, and M. P. Tornai, "Investigation of cone-beam acquisitions implemented using a novel dedicated mammotomography system with unique arbitrary orbit capability," *Proc. SPIE* **5745**, 609–617 (2005).
- ²⁵R. L. McKinley, E. Samei, C. N. Brzymialkiewicz, M. P. Tornai, and C. E. Floyd, "Measurements of an optimized beam for x-ray computed mammotomography," *Proc. SPIE* **5368**, 311–319 (2004).
- ²⁶R. L. McKinley and M. P. Tornai, "Preliminary investigation of dose for a dedicated mammotomography system," *Proc. SPIE* **6142**, 08.1–08.11 (2006).
- ²⁷R. L. McKinley et al., "Analysis of a novel offset cone-beam transmission imaging system geometry for accommodating various breast sizes," *Physica Medica* **21**, 48–55 (2006).
- ²⁸R. L. McKinley, M. P. Tornai, C. N. Brzymialkiewicz, P. Madhav, E. Samei, and J. E. Bowsher, "Analysis of a novel offset cone-beam transmission imaging system for attenuation correction of SPECT in a proposed dual modality dedicated breast mammotomography system," presented at the Workshop on the Nuclear Radiology of Breast Cancer, Rome, Italy, 22–23 October (2004).
- ²⁹R. L. McKinley, M. P. Tornai, E. Samei, and M. L. Bradshaw, "Initial study of quasi-monochromatic beam performance for x-ray computed mammotomography," *IEEE Trans. Nucl. Sci.* **52**, 1243–1250 (2005).
- ³⁰R. L. McKinley, M. P. Tornai, E. Samei, and M. L. Bradshaw, "Simulation study of a quasi-monochromatic beam for x-ray computed mammotomography," *Med. Phys.* **31**, 800–813 (2004).
- ³¹D. J. Crotty, P. Madhav, R. L. McKinley, and M. P. Tornai, "Patient bed design for an integrated SPECT-CT dedicated mammotomography system," *Nuclear Science Symposium Conference Record*, 2006 (IEEE, New York, 2006), Vol. 6, pp. 3915–3919.
- ³²B. Chen and R. Ning, "Cone-beam volume CT mammographic imaging: Feasibility study," *Med. Phys.* **29**, 755–770 (2002).
- ³³R. Ning et al., "Evaluation of flat panel detector cone beam CT breast imaging with different sizes of breast phantoms," *Proc. SPIE* **5745**, 626–636 (2005).
- ³⁴R. Ning, X. Tang, and D. Conover, "X-ray scatter correction algorithm for cone beam CT imaging," *Med. Phys.* **31**, 1195–1202 (2004).
- ³⁵R. Ning, X. Tang, and D. L. Conover, "X-ray scatter suppression algorithm for cone beam volume CT," *Proc. SPIE* **4682**, 774–781 (2002).
- ³⁶R. Ning et al., "Preliminary system characterization of flat-panel-detector-based cone-beam CT for breast imaging," *Proc. SPIE* **5368**, 292–303 (2004).
- ³⁷S. J. Glick, "Breast CT," *Annu. Rev. Biomed. Eng.* **9**, 501 (2007).
- ³⁸X. Gong, S. J. Glick, B. Liu, A. A. Vedula, and S. Thacker, "A computer simulation study comparing lesion detection accuracy with digital mammography, breast tomosynthesis, and cone-beam CT breast imaging," *Med. Phys.* **33**, 1041–1052 (2006).
- ³⁹X. Gong, A. A. Vedula, S. Thacker, and S. J. Glick, "A comparison of lesion detection accuracy using digital mammography and flat-panel CT breast imaging," *Proc. SPIE* **5745**, 860–869 (2005).
- ⁴⁰C. Lai et al., "Visibility of microcalcification in cone beam breast CT: Effects of x-ray tube voltage and radiation dose," *Med. Phys.* **34**, 2995–3004 (2007).
- ⁴¹L. Chen et al., "Cone-beam CT breast imaging with a flat panel detector: A simulation study," *Proc. SPIE* **5745**, 943–951 (2005).
- ⁴²Q. Xia, "Dedicated computed tomography of the breast: Image processing and its impact on breast mass detectability," Ph.D. thesis, Duke University, 2007.
- ⁴³J. Xia, J. Lo, K. Yang, C. E. Floyd, and J. Boone, "Dedicated breast computed tomography: Volume image denoising via a partial-diffusion equation based technique," *Med. Phys.* **35**, 1950–1958 (2008).
- ⁴⁴M. C. Altunbas et al., "A post-reconstruction method to correct cupping artifacts in cone beam breast computed tomography," *Med. Phys.* **34**, 3109–3118 (2007).
- ⁴⁵N. Packard and J. M. Boone, "Glandular segmentation of cone beam breast CT volume images," *Proc. SPIE* **6510**, 38.1–38.8 (2007).
- ⁴⁶C. M. Li et al., "Three-dimensional computer generated breast phantom based on empirical data," *Proc. SPIE* **6913**, 14.1–14.8 (2008).
- ⁴⁷U.S. National Bureau of Standard, *Report of the task group on reference man: Anatomical values for reference man* (1975).
- ⁴⁸J. M. Boone, "Normalized fibroglandular dose (DgN) coefficients for arbitrary x-ray spectra in mammography: Computer-fit values of Monte Carlo derived data," *Med. Phys.* **29**, 869–875 (2002).
- ⁴⁹P. R. Bakic, M. Albert, D. Brzakovic, and A. D. A. Maidment, "Mammogram synthesis using a 3D simulation. II. Evaluation of synthetic mammogram texture," *Med. Phys.* **29**, 2140–2151 (2002).
- ⁵⁰C. B. Caldwell et al., "Characterization of mammographic parenchymal pattern by fractal dimension," *Phys. Med. Biol.* **35**, 235–247 (1990).
- ⁵¹J. W. Byng, N. F. Boyd, E. Fishell, R. A. Jong, and M. J. Yaffe, "Automated analysis of mammographic densities," *Phys. Med. Biol.* **41**, 909–923 (1996).
- ⁵²M. Aguilar, E. Anguiano, and M. Pancorbo, "Fractal characterization by frequency analysis: II. A new method," *J. Microsc.* **172**, 233–238 (1993).
- ⁵³E. Anguiano, M. Pancorbo, and M. Aguilar, "Fractal characterization by frequency analysis: I. Surfaces," *J. Microsc.* **172**, 223–232 (1993).
- ⁵⁴G. D. Tourassi, D. M. Delong, and C. E. Floyd, Jr., "A study on the computerized fractal analysis of architectural distortion in screening mammograms," *Phys. Med. Biol.* **51**, 1299–1312 (2006).
- ⁵⁵J. I. Chen et al., "Fractal analysis of trabecular patterns in projection radiographs," *Invest. Radiol.* **29**, 624–629 (1994).
- ⁵⁶J. J. Heine and R. P. Velthuisen, "A statistical methodology for mammographic density detection," *Med. Phys.* **27**, 2644–2651 (2000).

***In vivo* characterization of breast tissues through absolute attenuation coefficients using dedicated cone-beam CT**

Priti Madhav^{1,2}, Christina M. Li^{1,2}, Olav I. Christianson^{2,3}, Martin P. Tornai^{1,2,3}

¹ *Department of Biomedical Engineering, Duke University, Durham, NC 27710*

² *Department of Radiology, Duke University Medical Center, Durham, NC 27710*

³ *Medical Physics Graduate Program, Duke University Medical Center, Durham, NC 27710*

With advances in 3D *in vivo* imaging technology, non-invasive procedures are being used to characterize tissues to identify tumors and monitor changes over time. Using a dedicated breast CT system with a quasi-monochromatic x-ray source and flat-panel digital detector, this study was performed in an effort to directly characterize different materials *in vivo* based on their attenuation coefficients. CT acquisitions were acquired using a rod phantom having different materials (delrin, polyethylene, acrylic, glandular-equivalent, and fat-equivalent) and a human cadaver breast embedded with spherical acrylic lesions. Projections were collected with and without a beam stop array. For each projection, 2D scatter was estimated by cubic spline interpolating the average values behind the shadow of each beam stop inside the object. Scatter-corrected projections were then calculated by subtracting the scatter images containing only a mask of the object from corresponding projections without the beam stops. Iterative OSTR was used to reconstruct the data and estimate the non-uniform attenuation distribution. An additional post-reconstruction flattening technique was applied to further reduce image non-uniformity. Preliminary results show that scatter correction reduces cupping artifact, improves image contrast, and yields attenuation coefficients closer to narrow-beam values. Peaks in the histogram showed clear separation among different material attenuation coefficients. Although post-reconstruction flattening did not improve contrast, its combination with the scatter correction further reduced the visual cupping artifact. These findings indicate that minimizing beam hardening with a quasi-monochromatic x-ray beam and applying scatter correction make it practical to directly characterize different tissues *in vivo* using absolute attenuation coefficients.

This work is supported by NIH grant RO1-CA096821, and partly by DOD grants W81XWH-06-1-0791 and W81XWH-06-1-0732.

KEYWORDS: Computed mammotomography, breast CT, cone-beam, OSTR, scatter, beam stop array, tissue classification, absolute attenuation coefficient

***In vivo* characterization of breast tissues through absolute attenuation coefficients using dedicated cone-beam CT**

Priti Madhav, Christina M. Li, Olav I. Christianson, Martin P. Tornai

PURPOSE: With advances in 3D *in vivo* imaging technology, non-invasive procedures are being used to characterize distinct tissues. Distinguishing different tissue compositions can be useful in identifying disease from normalcy, as well as observing changes over time with response to therapy. The Multi-Modality Imaging Lab at Duke University developed a dedicated breast CT system that uses a quasi-monochromatic x-ray source and a flat-panel digital x-ray detector to provide high quality volumetric data. In this study, scatter correction is implemented to obtain quantifiable reconstructed CT images. Minimizing beam hardening (due to the quasi-monochromatic x-ray source) and applying scatter correction can enhance image visualization and allow for direct *in vivo* characterization of different tissue types based on measured attenuation coefficients.

METHODS: Experiments were conducted with the CT sub-system of the dual-modality dedicated breast SPECT-CT scanner.¹ The CT component uses a rotating tungsten target x-ray source (model Rad-94, *Varian Medical Systems*, Salt Lake City, UT) with a 0.4/0.8mm nominal focal spot size and 14° anode angle and a 20×25cm² FOV CsI(Tl)-based amorphous silicon digital x-ray detector (model Paxscan 2520, *Varian Medical Systems*, Salt Lake City, UT) with a grid size of 1920 × 1536 pixels and 127μm pitch. A custom-built collimator is attached to the x-ray source to hold ultra-thick K-edge beam shaping filters to produce a quasi-monochromatic beam.² For these studies, a 60kVp x-ray beam with a 2.5mAs exposure per projection and a 0.051cm cerium filter ($Z = 58$, $\rho = 6.77 \text{ g cm}^{-3}$, K-edge = 40.4keV, *Santoku America, Inc.*, Tolleson, AZ) were used. This filter yielded a spectrum that had a mean energy of approximately 36keV and the FWHM of 15%. The source-to-image distance (SID) is 60cm and source-to-object distance (SOD) is 38cm resulting in a magnification of 1.57 for an object located at the center of rotation of the system. This study is done using a rod phantom with different materials including delrin, polyethylene, acrylic, and glandular-equivalent and fat-equivalent plastics (*Computerized Imaging Reference Systems, Inc.*, Norfolk, VA) (FIG. 1 and TABLE 1), and a human cadaver breast embedded with acrylic spheres to mimic small, low contrast lesions. All projections were corrected for gain and offset and binned to 4x4 pixels. For each phantom, projections were collected with and without a beam stop array (BSA) (FIG. 2, LEFT and MIDDLE). The BSA was a 9.5x9.5x2cm acrylic plate that consisted of 108 2mm diameter lead balls spaced 5mm apart on a Cartesian grid. It was placed in front of the collimator (~15cm from the x-ray source). The algorithm to determine the scatter distribution using the BSA was based upon a technique found in the literature.³ A 2D scatter distribution for each projection was estimated by cubic spline interpolating the measured average values located behind the shadow of each beam stop inside the object (FIG.2, MIDDLE). The final scatter-corrected projections were then calculated by subtracting the scatter images containing only a mask of the object (FIG.2, RIGHT) from the original corresponding projections without the beam stops. Reconstructions were done using a ray-driven iterative ordered-subset transmission reconstruction algorithm (OSTR) which provided an estimate of the non-uniform attenuation distribution of the object. Reconstruction parameters were set to 10 iterations, 16 subsets, 350x350x384 reconstruction grid, and 508μm³ voxel size. A post-reconstruction flattening technique was additionally applied to the images to make them appear smoother in each coronal slice.^{4, 5} Data analysis was done by plotting line profiles and viewing image histograms for four different reconstruction sets: (1) no corrections (NC); (2) only scatter correction (SC); (3) only post-reconstruction flattening correction (PRF); and (4) scatter and post-reconstruction flattening correction (SC-PRF). Measured attenuation coefficients from the reconstructed images were compared with actual narrow-beam values calculated at the same energy.⁶

RESULTS: The dedicated CT system provides high quality volumetric images with clear depiction of differentiated breast tissues and internal structure (FIG. 3-4). A histogram of an uncorrected reconstructed CT slice acquired from a human subject volunteer is shown in Fig. 4. Use of the quasi-monochromatic x-ray source makes it possible to distinctly separate the breast tissue composition into fat, glandular, and (surgically confirmed) lesion. Fig. 5 shows that the measured scatter correction reduces the cupping artifact, improves image contrast, and yields attenuation coefficients closer to narrow-beam values. Peaks in the histogram showed distinct separation among different materials. Although the post-reconstruction flattening technique did not improve image contrast, its combination with the scatter correction method helped further reduce the cupping artifact, which does have an impact on image quality. The flattening technique also degraded the separation of the object components.

NEW OR BREAKTHROUGH WORK: Along with the implementation of CT scatter correction in the iterative framework and the use of the quasi-monochromatic x-ray cone beam, this dedicated breast CT scanner makes it possible

for direct *in vivo* characterization of breast tissue by distinguishing and measuring absolute attenuation coefficients in the final reconstructed images. This can assist in identifying normal and diseased tissues and in monitoring changes that might occur over time with or without therapy.

CONCLUSIONS: Preliminary results demonstrate that with the implementation of a quasi-monochromatic x-ray source, scatter correction and iterative reconstruction, CT reconstructed images can yield attenuation coefficients of different materials close to their actual narrow-beam values. This can lead to direct *in vivo* characterization of tissue without invasive procedures and allow better differentiation between materials with similar attenuation coefficients.

PREVIOUS SUBMISSION OF THIS WORK: None

REFERENCES

¹ P. Madhav, D. J. Crotty, R. L. McKinley and M. P. Tornai, "Evaluation of tilted cone-beam CT orbits in the development of a dedicated hybrid mammotomograph," *Phys Med Biol* **54**, 3659-3676 (2009).
² D. J. Crotty, R. L. McKinley and M. P. Tornai, "Experimental spectral measurements of heavy K-edge filtered beams for x-ray computed mammotomography," *Phys Med Biol* **52**, 603-616 (2007).
³ J. Y. Lo, C. E. Floyd, Jr, J. A. Baker and C. E. Ravin, "Scatter compensation in digital chest radiography using the posterior beam stop technique," *Med. Phys.* **21**, 435-443 (1994).
⁴ M. C. Altunbas, C. C. Shaw, L. Chen, et al., "A post-reconstruction method to correct cupping artifacts in cone beam breast computed tomography," *Med Phys* **34**, 3109-3118 (2007).
⁵ C. M. Li, W. P. Segars, G. D. Tourassi, J. M. Boone and J. T. Dobbins. III, "Methodology for generating a 3D computerized breast phantom from empirical data," *Medical Physics* **36**, 3122-3131 (2009).
⁶ J. H. Hubbell and S. M. Seltzer, "Tables of x-ray mass attenuation coefficients and mass energy-absorption coefficients 1keV to 20MeV for elements Z=1 to 92 and 48 additional substances of dosimetric interest," *Journal* (1996).

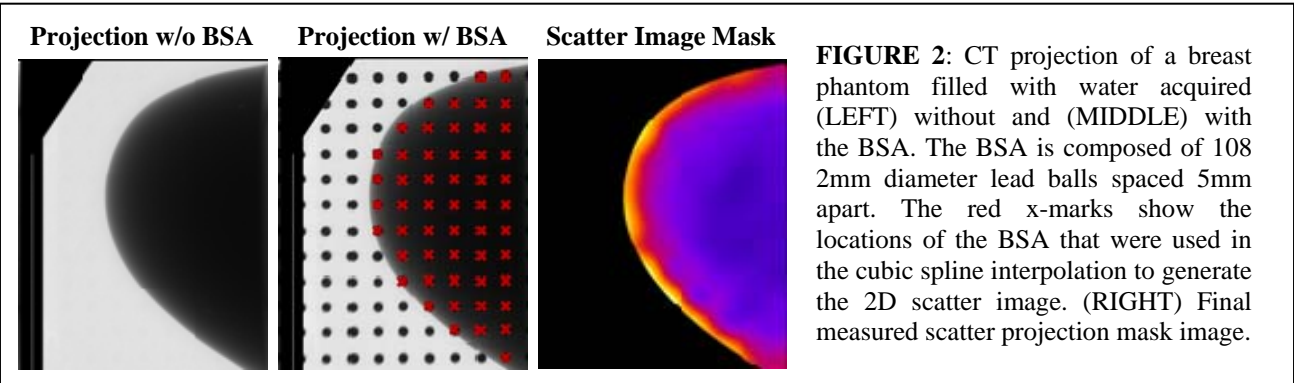
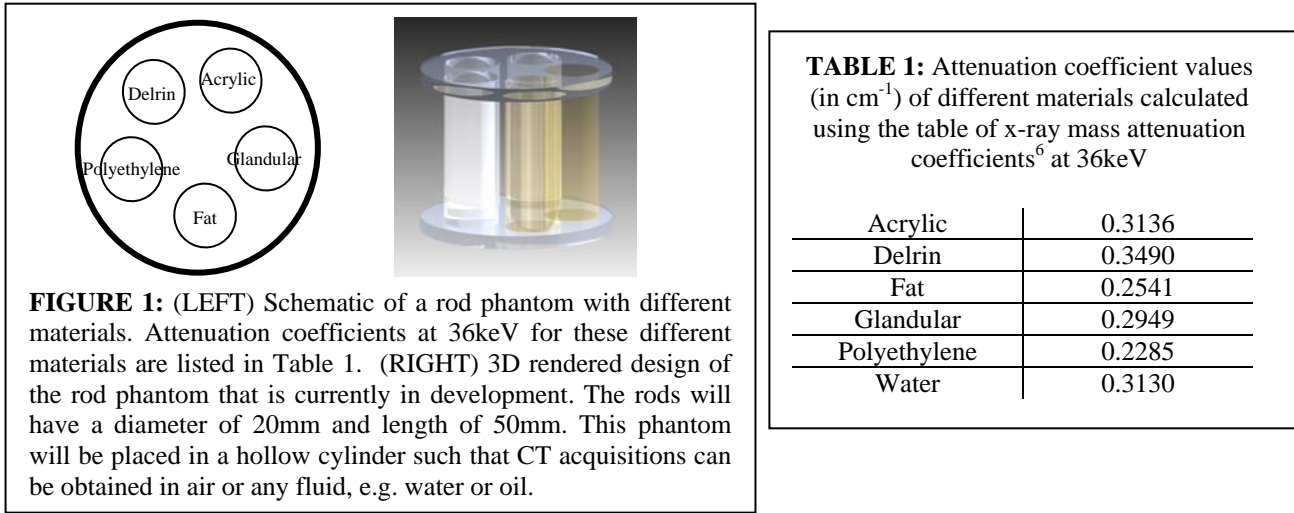




FIGURE 3: (LEFT) Photograph of a cadaver breast from a 48-year old woman placed inside a breast phantom shell. (RIGHT) Uncorrected reconstructed CT coronal slice through the breast shows clear distinction between the fat and glandular tissue.

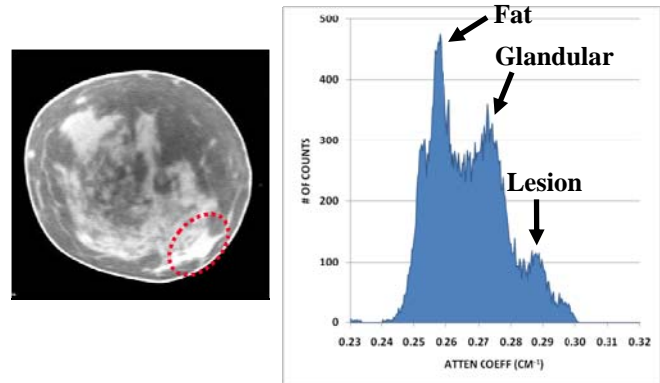


FIGURE 4: (LEFT) Uncorrected reconstructed CT coronal slice of a 45-year post-menopausal woman with biopsy confirmed breast cancer. Surgically confirmed lesion is indicated within the red dotted circle. (RIGHT) Image histogram of this single slice shows a clear distinction among the attenuation coefficients for the different tissues. This differentiation is due to the quasi-monochromatic x-ray source that the CT system uses.

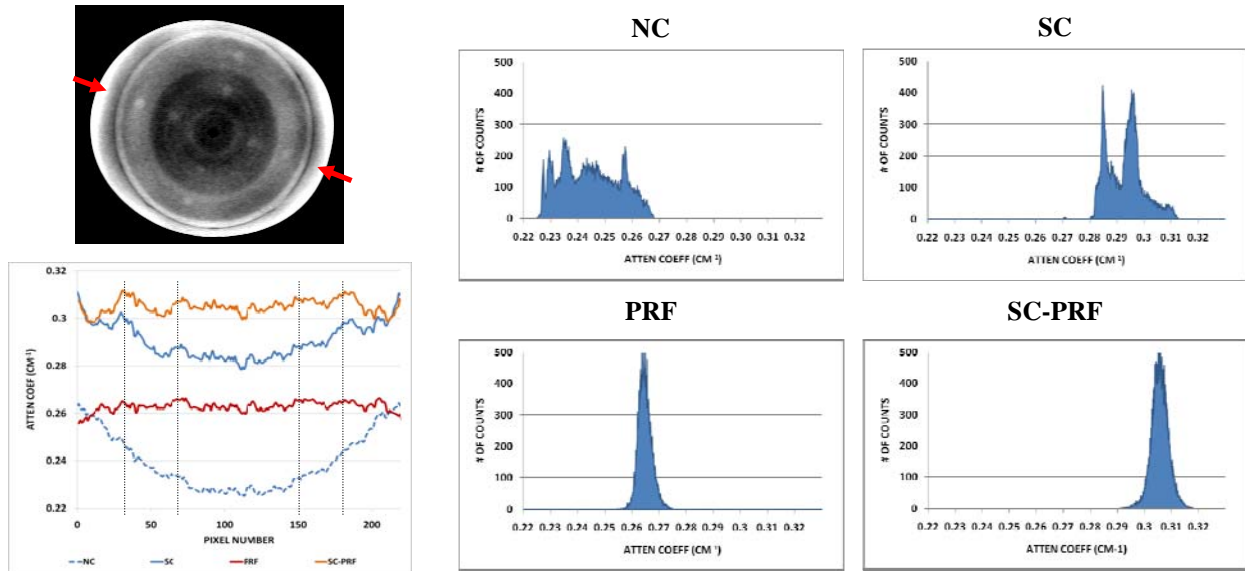


FIGURE 5: (LEFT TOP) Scatter-corrected only (SC) reconstructed CT coronal slice of a breast phantom shell filled with water and acrylic balls arranged in a cross pattern. A tight window was applied to the image such that the acrylic balls could be clearly seen in the water background. (LEFT BOTTOM) Line profile through the acrylic lesions (between the red arrows) for all four reconstruction sets: no corrections (NC); only scatter correction (SC); only post-reconstruction flattening correction (PRF); and scatter and post-reconstruction flattening correction (SC-PRF). Profile shows that scatter correction reduces the cupping artifact, improves the contrast between acrylic and water, and yields attenuation coefficient values close to the narrow-beam values (see Table 1). The vertical dashed lines indicate the location of the center of each acrylic sphere. The post-reconstruction flattening correction helped to further reduce the cupping artifact. (RIGHT) Image histograms of all four reconstruction sets. With only scatter correction, the histogram shows two distinct peaks. Adding the post-reconstruction flattening correction degrades the histogram by showing a single peak close to 0.31cm^{-1} .